Energy & Environmental Science

Accepted Manuscript

ROYAL SOCIETY OF CHEMISTRY

www.rsc.org/ees

An exploration of the compositional space for mixed lead halogen perovskites for high efficiency solar cells

T. Jesper Jacobsson[1]*, Juan-Pablo Correa-Baena[1], Meysam Pazoki[2], Michael Saliba[3], Kurt Schenk[4], Michael Grätzel[3], and Anders Hagfeldt*[1,2]

1) Laboratory for Photomolecular Science, Institute of Chemical Sciences and Engineering, École Polytechnique Fédérale de Lausanne, CH-1015-Lausanne, Switzerland
2) Department of Chemistry - Ångström Laboratory, Uppsala University, Box 538, 75121 Uppsala, Sweden
3) Laboratory of Photonics and Interfaces, Institute of Chemical Sciences and Engineering, École Polytechnique Fédérale de Lausanne, CH-1015-Lausanne, Switzerland
4) École Polytechnique Fédérale de Lausanne, CH-1015-Lausanne, Switzerland

Jacobsson.jesper.work@gmail.com
+46 70 5745116
Anders.hagfeldt@epfl.ch
+41 (0)21 693 53 08

Table of content image

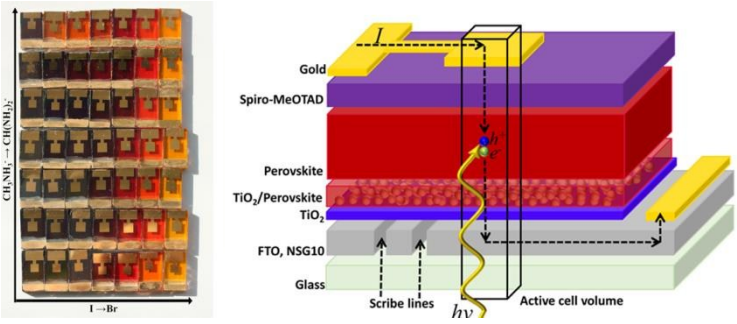

A systematic investigation of the compositional space for perovskite solar cells spanned by $MAPbI_3$, $MAPbBr_3$, $FAPbI_3$ and $FAPbBr_3$

Abstract

Lead halide perovskites have attracted considerable interest as photo absorbers in PV-applications over the last few years. The most studied perovskite material achieving high photovoltaic performance has been methyl ammonium lead iodide, $CH_3NH_3PbI_3$. Recently the highest solar cell efficiencies have, however, been achieved with mixed perovskites where iodide and methyl ammonium partially have been replaced by bromide and formamidinium. In this work, the mixed perovskites were explored in a systematic way by manufacturing devices where both iodide and methyl ammonium gradually were replaced by bromide and formamidinium. The absorption and the emission behavior, as well as the crystallographic properties were explored for the perovskites in this compositional space. The band gaps as well as the crystallographic structures were extracted. Small changes in the composition of the perovskite were seen to have a large impact on the material properties and the device performance. In the investigated compositional space, cell efficiencies do, for example, vary from a few percent up to 20.7%. From the perspective of applications, exchanging iodide with bromide is especially interesting as it allows a tuning of the band gap from 1.5 to 2.3 eV. This is highly beneficial for tandem applications, and an empirical expression for the band gap as a function of composition was determined. Exchanging a small amount of iodide with bromide is found to be highly beneficial whereas a larger amount of bromide in the perovskite was found to cause intense sub band gap photoemission with detrimental results for the device performance. This could be caused by formation of a small amount of an iodide rich phase with a lower band gap, even though such a phase was not observed in diffraction experiments. This shows that stabilizing the mixed perovskites will be an important task to get the higher band gap bromide rich perovskites to reach the high performances seen for the best compositions.

Key words

Lead halide perovskites, $CH_3NH_3PbI_3$, $CH_3NH_3PbBr_3$, $CH(NH_2)_2PbI_3$, $CH(NH_2)_2PbBr_3$, $MAPbI_3$, $MAPbBr_3$, $FAPbI_3$, $FAPbBr_3$, solar cells, PV, perovskites, mixed perovskites, phase segregation, photoluminescence.

Broader context

The world is now slowly starting to grasp the consequences of a greenhouse gas driven anthropogenic warming of the climate system while, simultaneously, the available reserves of fossil fuels are in decline. At the same time, we also experience an unprecedented expansion of renewable energy production. The fastest growing field of renewable energy production is photovoltaics. At the moment this market is dominated by silicon solar cells but there are several interesting alternatives, such as lead halogen perovskites which have attracted considerable interest in the last years with efficiencies surpassing 20 % in only half a decade of research. The perovskite most frequently investigated so far is methyl ammonium lead iodide, $CH_3NH_3PbI_3$, but both the organic and the halide ions can be exchanged and the best cells at the moment are based on perovskites with a mixed composition of methyl ammonium, formamidinium, iodide, and bromide. The compositional space for these mixtures is still rather underexplored, both with respect to the underlying physics and with respect to optimized device performance. The most promising initial application for the perovskites is not as standalone cells but as a top cell in a tandem architecture together with conventional silicon cells. This makes the gradual exchange of iodide to bromide especially interesting as it allows a fine tuning of the band gap of the perovskite. In this paper, we present a systematic study of the compositional space of methyl ammonium/formamidinium and iodide/bromide perovskites. We show both high efficiency devices and illuminate problems of sub band gap emission and possible phase segregation for high band gap perovskites that need further research before they could be used in tandem applications.

Introduction

Recently, lead halogen perovskites have attracted considerable interest as photo absorbers for solar cell applications. The first reports on these materials dates back to 1978[1, 2], and they have a number of possible optoelectronic applications including bright light emitting diodes[3], lasers[4, 5], and photo-detectors[6]. It is, however, as photovoltaic materials where they have gained the most attention. The first paper using these perovskites for PV-applications was published in 2009 by Kojima et al[7]. The efficiencies of the first devices were low and they were highly unstable. After a number of advances regarding material synthesis and device engineering during the following years[8-12], the field expanded rapidly and the top efficiencies have now reached 21 %[13]. These high efficiencies, together with the prospect of cheap precursors and versatile synthesis methods, makes the perovskites real candidates for a competitive solar cell technology; either as standalone cells or as top cells in a tandem configuration with conventional solar cells.

The lead halogen perovskites have the general formula $APbX_3$, where A is an organic cation and X is a halogen ion. So far, the most investigated perovskite is $CH_3NH_3PbI_3$, or $MAPbI_3$, where A is methyl ammonium, MA, and X is iodide. That can be considered as the current standard perovskite and the baseline from which subsequent changes take place. $MAPbI_3$ is, however, not a single golden compound but rather a representative of a larger class of related compounds.

The methyl ammonium (MA) ions have been replaced with other organic ions, most often formamidinium (FA), $CH(NH_2)_2^+$, which has showed good results[14-17]. FA is somewhat larger than MA which results in a cubic structure with a slightly larger lattice, and a band gap that is a bit lower and is closer to the optimal band gap for a single junction cell. For $FAPbI_3$, efficiencies up to 20 % have been reported[17] but there is a problem with stability as the $FAPbI_3$ is prone to transform into a yellow polymorph which is not suitable for solar cell applications[14]. Several studies have shown that by mixing MA and FA, the problem of transformation to the yellow polymorph is avoided and good cells have been produced[15, 18, 19]. MA has also been exchanged by caesium ions[20]. These fully inorganic perovskites are interesting but are so far, in terms of efficiencies, outperformed by their hybrid counterparts. Partial replacement with caesium has, however, showed decent results[21-23]

The iodide has been replaced by other halides, i.e. chloride[24] and bromide[25]. The iodide can gradually be replaced by bromide which has been demonstrated for both the methyl ammonium perovskites[26-28] and for the formamidinium analogues[29]. This transitions change the band gap from approximately 1.5 to 2.3 eV. In principle, the same gradual transition may be possible by chloride substitution where even higher band gaps are possible. In practice, chloride substitution has been difficult[30] and at the moment, the I/Br-system appears to be more promising and is therefore the focus of this paper.

It is also possible to simultaneously change the MA/FA and Br/I-ratios[17, 31, 32] and the last three certified records in the NREL-chart[33] are based on these mixed perovskites where the best cells have some of the iodine replaced with bromide and most of the MA replaced by FA. It is still not determined what the best composition would be, and why some compositions would be better than others are still unclear and requires further investigations, which takes us to the core of this work. In this work, for the first time, the compositional space of the MA/FA-Pb-I/Br perovskite system is systematically explored. That is done by simultaneously, and independently, changing the MA/FA and the I/Br-ratios in the precursor solutions used in the synthesis. Both the perovskite materials as well as final devices were made and analyzed in order to improve our understanding for this parameter space.

There are basically two reasons to why the mixed perovskites are of particular interest. The first is about efficiencies and stabilities, which both must be high for standalone perovskite cells to be of real technological interest, and at the moment the mixed perovskites appears to be a way forward towards reaching those goals. The other reasons for the interest in the mixed perovskites is tandem applications, where the possibility of tuning the band gap is highly appealing. A likely initial road for the commercialization of perovskites for solar cell applications is not as standalone cells but as an add-on to silicon or other commercial solar cell technologies where the perovskite would be the top cell in a tandem architecture[34, 35]. Recently, some efforts have been directed towards that goal[35-40] and there are several benefits with such an approach. To act as a standalone technology, the perovskite would need to match silicon, which is hard given the position silicon have in terms of efficiency, large scale production, installation etc. In a tandem architecture, some demands are reduced and by combining a decent silicon cell with a decent perovskite cell, something that performs better than top quality silicon is achievable[37, 38]. As one of the main driver for overall cost reduction in silicon solar cells is to increase the cell efficiency, such a solution gives a favorable economics to the problem. At the same time, the perovskite could ride upon the established silicon technology and thereby prove itself for further applications. The ideal band gap for a top cell together with silicon, which has a band gap of 1.1 eV, would be 1.72 eV, and for a pure perovskite tandem the ideal band gaps would be around 1.55 and 2.05 eV given some reasonable assumptions elaborated further down in this paper.

Investigating the physics of the mixed iodine/bromide perovskites is thus highly relevant as it both may provide more efficient perovskite solar cells as well as perovskites with tailored band gaps suitable for tandem applications. It is reasonable to expect that the properties of the mixed perovskites will deviate from the pure $MAPbI_3$-perovskite and that the optimized synthesis protocols will do so as well.

The paper starts with a methods section detailing the experimental and computational procedures used. The analysis of the experimental data involves: optical absorption, photoluminescence, X-ray diffraction, morphological investigations, and IV-characteristics for the full set of devices. This is complemented by theoretical DFT calculations, which give the relative energetics for the four corner compounds. The crystallographic properties and the requirements for tandem architectures are also reviewed briefly. At the end we discuss the implications of our results for manufacturing of high efficiency devices, band gap tuning for tandem devices, and possible phase segregation in mixed perovskites.

Experimental methods

Perovskite and device preparation

As substrate for the devices, FTO NSG 10 was used. The substrates were cleaned in freshly prepared piranha solution composed of five parts concentrated H_2SO_4 and two parts 30 % H_2O_2. Proper protection should be used while handling this solution as it is highly aggressive and preparing it is an exothermic process. The substrates were soaked in the piranha solution for 10 minutes and then rinsed, first in water and finally in ethanol. They were thereafter treated in a UV-ozone cleaner for 10 minutes.

A hole blocking layer of TiO_2 was deposited on the cleaned FTO substrates using spray pyrolysis. The spray solution was composed of ethanol, acetyl acetone, and titanium diisopropoxide (30% in isopropanol) in the proportions 90:4:6 by volume. Oxygen at a base pressure of 1 bar was used as a carrier gas. The glass substrates were heated to 450°C on a hotplate and kept at that temperature for 15 minutes prior to the spraying. After an additional

30 minutes at 450°C, the sprayed glass substrates were slowly cooled to room temperature. 10 ml of spray solution was used to cover 40 cm^2 of substrates. This procedure gives a compact layer of anatase with a thickness of around 20-30 nm.

On top of the compact TiO_2-layer deposited by spray pyrolysis, a mesoporous scaffold of TiO_2 nanoparticles was deposited by spin-coating. TiO_2 paste (Dyesol 30 NR-D) was bought from Dyesol and was dissolved in ethanol at a concentration of 150 mg/mL. On each substrate (1.4·2.4 cm) 50 µL of the TiO_2 solution was applied and spin-coated at 4000 rpm, with an acceleration of 2000 rpm/s, for 10 s. A piece of scotch tape was used on one side of the substrates to prevent the mesoporous TiO_2 to form where the front contacts were to be deposit. The substrates with mesoporous TiO_2 were sintered at 450ºC in air on a hot plate for 30 minutes and then slowly cooled to ambient temperature.

For XRD-measurements, the perovskites were deposited on soda lime glass (SLG) covered by 15 nm amorphous SnO_2. The SnO_2 film increases the wettability of the precursor solutions which give perovskite films of higher quality. The SnO_2 was deposited by atomic layer deposition, ALD, at 120°C using a Savanah ALD 100 from Cambridge Nanotech Inc. As a tin precursor, Tetrakis(dimethylamino)tin(IV), bought from Stem Chemicals Inc., was used. Ozone was used as the oxidising agent. The ozone was produced by an ozone generator fed with oxygen gas (99.9995% pure, Carbagas) producing O_3 at a concentration of 13% in O_2. Nitrogen was used as a carrier gas with a flow rate of 5 sccm. The substrates with SnO_2 were directly prior to perovskite deposition treated in a UV-ozone cleaner for 10 minute. This process for deposition an electron selective SnO_2 contact is described in more detail in a previous publication[31], and has been used as an electron selective contact in high efficiency planar devices[31].

Prior to perovskite deposition, the substrates with mesoporous TiO_2 underwent a lithium treatment which has been found to be beneficial for the device performance[41]. On the substrates, 100 µL of a 35mM Lithium bistrifluoromethanesulfonimidate, Li-TFSI, in acetonitrile was applied and thereafter the substrates were spun at 3000 rpm for 10 s. The substrates were then thermally annealed in air at 450°C for 30 minutes and then slowly cooled to 150ºC, where after they were brought directly into a glovebox for perovskites deposition.

A total of 49 precursor solutions with varying concentrations of PbI_2, $PbBr_2$, CH_3NH_3I, CH_3NH_3Br, $CH(NH_2)_2I$, and $CH(NH_2)_2Br$ were used for perovskite preparation. For all samples, the total lead concentration, [Pb^{2+}], in the final precursor solution was held at 1.25 M. That is the optimised concentration used for the composition giving the highest efficiency devices previously produced in our lab[31]. In previous work, we have observed that a slight molar excess of PbI_2 with respect to ([MA] + [FA]) have been beneficial for device performance[42]. Why this is so is still not entirely understood even though a number of hypothesises have been presented based on passivation[43, 44], crystallisation dynamics[42] and charge transfer efficiency[42, 45]. Based on the previous results we made a design decision to have a molar excess of lead salts with respect to the organic ions for all the 49 compositions. The [Pb^{2+}] / ([MA] + [FA]) ratio for all precursor solutions was 1.1. The solvent used for the perovskite solutions was a mixture of anhydrous dimethyl formamide, DMF, and anhydrous dimethyl sulfoxide, DMSO in the proportion 4:1 by volume. A summary of the intended perovskite compositions and the corresponding sample number is given in figure 1, which also gives a graphical illustration of the compositional space here explored.

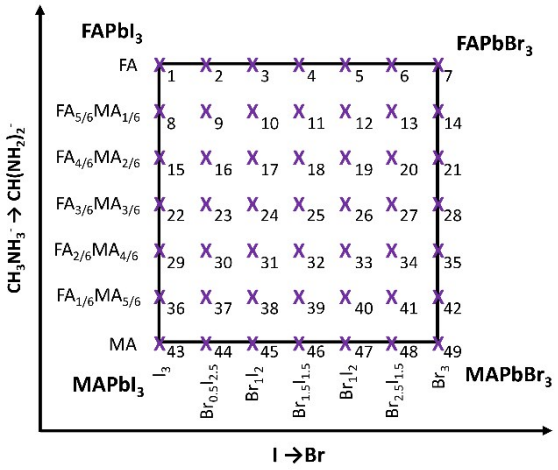

Figure 1. A graphical illustration of the compositional matrix with markings for all the compositions explored. The numbers next to the crosses represent the key between the intended perovskite compositions and sample numbers.

The solutions were prepared in a glovebox with nitrogen atmosphere. Stock solutions of PbI_2 and $PbBr_2$ were prepared in advance whereas the final precursor solutions were prepared just before perovskite deposition. Four master solutions were prepared; PbI_2 and CH_3NH_3I in DMF/DMSO, PbI_2 and $CH(NH_2)_2I$ in DMF/DMSO, $PbBr_2$ and CH_3NH_3Br in DMF/DMSO, and $PbBr_2$ and $CH(NH_2)_2Br$ in DMF/DMSO. These were mixed in the right proportions to get the 49 final precursor solutions. Tables of the exact composition and concentrations of all the species in the 49 solutions are given in the supporting information.

The MA and FA salts were bought from Dyesol and the lead salts were bought from TCI. All chemicals were used as received without further treatment. Due to the shear amount of samples, they were divided into seven separate batches.

The perovskites were spin-coated in a glove box with a flowing nitrogen atmosphere with a fairly high flow in order to ventilate out solvent vapors. For each sample, 35 µL of the precursor solution was spread over the substrate, which thereafter was spin-coated using a two-step program. The first step was a spreading step using a rotation speed of 1000 with an acceleration of 200 rpm/s rpm for 10 s. That step is immediately, without pause, followed by the second step where the films were spun at 4000 rpm for 30 s using an acceleration of 2000 rmp/s. During the second step, when approximately 15 seconds of the program remains, 100 µL of anhydrous chlorobenzene was applied on the spinning film with a hand held automatic pipette. This last step, known as the anti-solvent method, has a large impact on film morphology and result in significantly better device performance[46-48]. It is, however, one of the steps that introduce a palpable degree of artisanship into the process.

Directly after spin-coating, the films were placed on a hotplate at 100°C, where they were annealed between 30 and 70 min depending on the sample number. At this temperature, the transformation into the perovskite is visually seen to occur within the time frame of a minute. One exception is the pure $FAPbI_3$ perovskite (sample 1), which requires a higher annealing temperature to form. Those samples were annealed at 150°C.

After the heat treatment, the samples were cooled to ambient temperature where-after the solid-state hole-conductor was spin-coated on top of the films. A 70 mM solution of Spiro-MeOTAD (spiro) dissolved in chlorobenzene was used as a hole conductor. To improve the performance of the spiro, three different additives were added[49, 50]: 4-*tert*-butylpyridine, 1.8 M Li-TFSI in acetonitrile, and 0.25 M $Co[t\text{-}BuPyPz]_3[TFSI]_3$, also known as FK209, in acetonitrile. The Spiro:FK209:Li-Tfsi:TBP molar ratio was 1:0.05:0.5:3.3. The spiro solution was prepared the same day as the perovskite films were deposited.

The spiro was deposited by spin-coating at 4000 rpm for 20 s. 50 µL of the solution was deposited on the spinning film, using a hand held automatic pipet, a few seconds into the spinning program. The samples were stored in a desiccator pumped under vacuum for a day and the back contact was then deposited.

Before the back contact was deposited, the perovskite/spiro layer was removed from one end of the samples using a razorblade, acetonitrile, and a cotton bud in order to ensure contact between the FTO and the gold contact. The front and back contacts were composed of an 80 nm thick gold film deposited by physical vapor deposition at a pressure of around $2 \cdot 10^{-5}$ Torr using an evaporator from Leica, EM MED020.

Characterization

UV-vis absorption measurements were performed on an Ocean Optics spectrophotometer HR-2000 c with deuterium and halogen lamps. In all measurements, a full spectrum from 190 to 1100 nm with 2048 evenly distributed points was sampled. 100 consecutive spectra were averaged in order to obtain good statistics.

Steady state photoluminescence was measured with a Fluorolog, Horiba Jobon Yvon, FL-1065. A white tungsten lamp was used as luminous source, A monochromator was placed between the sample and the light source as well as between the sample and the detector. An excitation wavelength of 435 nm was used for all samples. The emission spectrum was measured from 455 nm to 835 nm in steps of one nm. An integration time of 0.5 s was used for each wavelength. Measurements were performed both on perovskites deposited on substrates with mesoporous TiO_2 and on films deposited on substrates with 15 nm amorphous SnO_2. The excitation source and the detector were placed in 90º with respect to each other. The sample was oriented 60° with respect to the excitation source in order to decrease interference form reflected light.

XRD measurements were measured using a Brucker diffractometer using a Bragg-Brentano geometry. $Cu_{k\alpha}$ radiation, with a wavelength of 1.54 Å, from a cupper target was used as X-ray source. 2θ scans between 10° and 65º were collected using a step size of 0.008º.

SEM imaging was carried out using a Zeiss Merlin scanning electron microscope. Photographs were taken using a Canon EOS 450 D with an EFS 60 macro lens.

The IV-characteristics of the devices were measured using a home built system. To simulate solar light, an Oriel solar simulator with a xenon arc lamp, fed with 450 W input power, was used together with a Schott K113 Tempax filter (Praäzisions Glas & Optik GmbH). The light intensity was calibrated with a silicon photodiode equipped with an IR-cutoff filter (KG3, Schott). The IV-curves were measured with a digital source meter (Keithley 2400). No equilibration time or light soaking was applied before the potential scan. The starting point for the measurements was chosen as the voltage where the cell provided approximately 2 mA in forward bias. From that point, the potential was scanned to short circuit and back again using a scan speed of 20 mV/s. Thereafter, the dark current was sampled using the same scan speed. The cells were masked with a metal mask in order to limit the active cell area to 0.16 cm^2. IV-curves measured on high efficiency devices with this setup have recently been confirmed to be in good agreement with data provided from independent certification agencies.

The external photocurrent efficiency, *EQE*, was measured on a subset of the samples. This was done by a home built system composed of a 300 W xenon lamp, a gemini-180 double monochromator and a lock in amplifier. A white bias light of 50 W/m^2 was provided by a LED array. The *EQE* for each wavelength was extracted by measuring the difference in short circuit current between the white bias light, and the white bias light together with a superimposed monochromatic light, and scaling the signal with the intensity of the monochromatic light. The monochromatic light was chopped at 2 Hz and to get reasonable

statistics, and a fairly long integration time was used. The *EQE* was measured in steps of 10 nm from 340 to 850 nm. The EQE- system has had some performance problems. Absorption onsets and relative intensities are trustworthy but too much significance should not be read into absolute values.

Computational methods

DFT calculations were performed on the four corner compositions, $MAPbI_3$, $MAPbBr_3$, $FAPbI_3$, and $FAPbBr_3$ in order to extract the density of states, DOS, and the partial density of states, PDOS. The intention of these computations is to provide anchoring points to be used while reasoning about the behavior of the mixed perovskites. Computations of the mixed perovskites are more complicated and outside of the scope of this particular paper, but is something we intend to address in later publications.

The crystal DFT calculations were performed using the General Gradient Approximation (GGA), exchange correlation functional, and the Perdew-Burke-Ernzerhof (PBE) pseudo-potential[51]. The lead $5d^{10}/6s^2/6p^2$, the nitrogen $2s^2/2p^3$, the iodide $5s^2/5p^5$, and the carbon $2s^2/2p^2$ electrons were considered as valence electrons. The super cells of all the four corner compositions were composed of 48 atoms placed in a tetragonal Bravais lattice with starting cell parameters, a = 8.71 Å and c = 12.46 Å. The orientation of the different methyl ammonium ions ($CH_3NH_3^+$) and formamidinium ions, ($CH_3(NH_2)_2^+$) were chosen in a way where neighboring dipoles were perpendicular to each other. This configuration has been reported to, according to DFT calculations, give a stable phase at room temperature; at least for the $MAPbI_3$[52, 53].

All the unit cell vectors and atom coordinates were relaxed to have a total force lower than 0.04 Ry/au. Cut-off energies for the plane wave function and the charge density were set to 30 and 300 Rydberg, respectively. Brillouin zone sampling was carried out by a 3x3x3 Monkhorst-Pack grid (MPG) for the relaxation procedure, a 4x4x4 MPG for the self-consistent procedures, and a 6x6x6 MPG for the non-self-consistent procedures.

Results and discussion

Optical absorption

The difference in perovskite compositions gives rise to a large variety in the optical appearance of the deposited films, as illustrated in the photo in figure 2**.** The compositions with iodine as the exclusive halide are dark brown and when the bromide content increases they successively become more red. When the bromide content gets close to 80%, they get a bright red color and when increased even further, the films get a clear yellow tone.

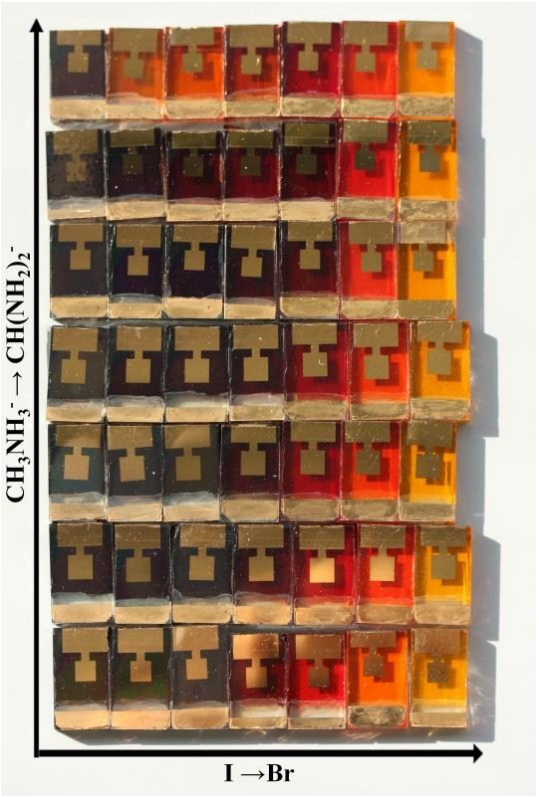

Figure 2. A photo of the favricated cells, with the Spiro-MeOTAD hole conductor and the gold contacts, showing the appearance in reflected light. The samples are arranged in the same way as in sample matrix in figure 1.

The absorption as a function of wavelength is given for a subset of the films in figure 3. The full set of figures is presented in the supporting information. In figure 3.a, the behavior upon changing the Br/I-ratio is illustrated. Higher bromide content results in a higher band gap, which is true regardless of the FA/MA-ratio. The band gap is, however, not the only thing that changes as also the shape of the absorption curve changes with halide composition. With higher bromide content, the absorption onset gets sharper and a peak in the absorption appears with the visual appearance of excitonic absorption. This excitonic absorption in the bromide rich perovskites has been observed before[29, 54] and is consistent with the higher excitoni binding energy reported for the bromide perovksites[55, 56].

The samples where FA is the only organic ion present, the absorption behavior are for a few samples distinctly different compared to the rest of the matrix. For those films, XRD data indicate that the hexagonal yellow polymorph[14] had formed as well.

While the organic ions are exchanged, the effect on the absorption is considerably smaller as illustrated in figure 3.b. That is in line with the theoretical calculations showing that the organic ions do not contribute significantly to the density of states close to the band edges. The calculated DOS curves for the four corner compounds are found in the supporting

information. There is, however, a slightly larger spread in the absorption behavior with respect to the organic ion when the amount of bromide and iodine is more or less the same. That could, however, be a result of film morphology rather than in the material itself.

The semitransparency is another factor that depends on the composition. This is illustrated in figure 3.c where the background due to light scattering in the absorption measurements is plotted as a function of composition. This data does not follow a strict trend, but there is a general tendency that the scattering is higher in the middle of the matrix. It is also higher for the samples where iodine is the only halide present.

SLG/SnO_2, FTO/SnO_2, and FTO/TiO_2/mesoporous-TiO_2 have here been used as substrates and this have not been seen to influence the absorption behavior.

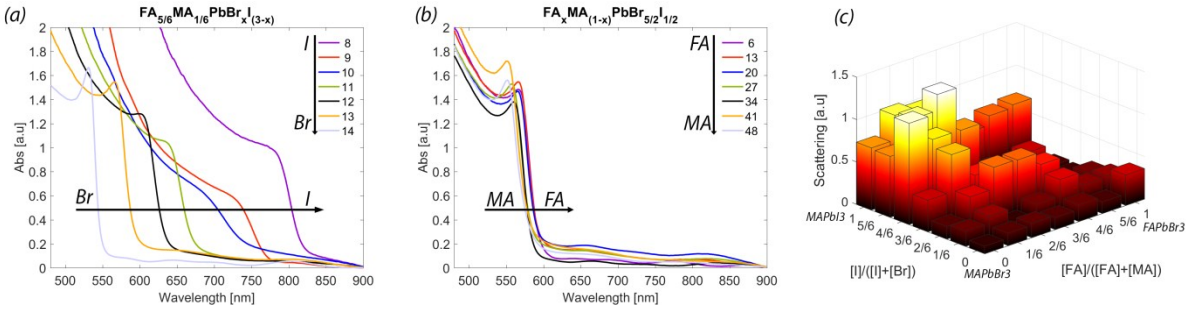

Figure 3. (a) Optical absorption as a function of wavelength for a subset of the samples, corresponding to samples 8-14, $FA_{5/6}MA_{1/6}PbBr_xI_{3-x}$ where the I/Br-ration is changed. The background due to scattering is removed. (b). Absorption for the subset of samples corresponding to $FA_xMA_{1-x}PbBr_{5/2}I_{1/2}$ where the MA/FA-ration was changed. (c) The height of the background in the absorption measurements as a function of composition.

Determining the band gap and its importance for tandem applications

The optical band gap was determined from the absorption data. This was done by subtracting the background caused by scattering and thereafter plotting the square of the absorption against photon energy. For direct semiconductors, the square of the absorption will be a linear function of the photon energy in a limited energy interval where the parabolic band approximation is valid, which it is in an energy region of up to a few hundred meV located above the band gap energy[57-59]. The band gap energy is given as the intercept with the baseline and the interpolation of this linear region, as illustrated for a few samples of different composition in figure 4.a. It should be pointed out that the nature of the excitonic absorption may result in a shift between the values extracted here and the true band gap, defined as the energy difference between the top of the valence band and the bottom of the conduction band in the undisturbed semiconductor. The values extracted here could be shifted by a value close to the exciton energy and may more correctly be considered as the absorption onset. The values extracted here are, however, from an operational perspective the more relevant parameter. The distribution of extracted band gaps in the compositional matrix is illustrated in figure 4.b, and the values are reported in table 1.

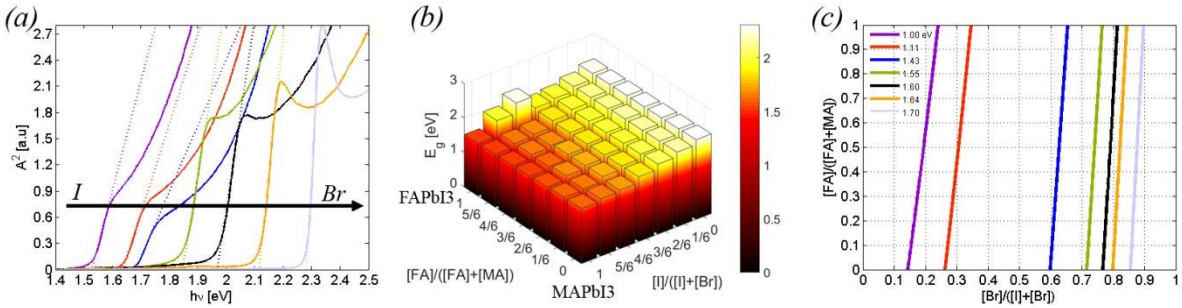

Figure 4. (a) Illustration of band gap determination for sample 15-21 which goes from no bromide to only bromide. Figures for the rest of the samples are given in the supporting information. (b) A bar plot of the band gaps in the compositional space explored. (c) Illustration of where in the explored compositional space the ideal band gap for a top cell is found with respect to the band gaps of several possible bottom cells.

Table 1. Band gap given in eV as a function of composition for the mixed perovskites.

Pb	I_3	$Br_{0.5}I_{2.5}$	Br_1I_2	$Br_{1.5}I_{1.5}$	$Br_2I_{1.}$	$Br_{2.5}I_{0.5}$	Br_3
FA	1.52	1.97	2.27	1.91	1.97	2.10	2.27
$FA_{5/6}MA_{1/6}$	1.53	1.63	1.68	1.87	1.98	2.11	2.28
$FA_{4/6}MA_{2/6}$	1.53	1.64	1.68	1.85	1.97	2.11	2.28
$FA_{3/6}MA_{3/6}$	1.55	1.61	1.75	1.85	1.96	2.14	2.28
$FA_{2/6}MA_{4/6}$	1.56	1.67	1.76	1.85	1.97	2.14	2.29
$FA_{1/6}MA_{5/6}$	1.59	1.63	1.76	1.86	1.99	2.15	2.30
MA	1.59	1.66	1.70	1.87	2.03	2.16	2.31

The most pronounced trend with respect to composition is an increase in the band gap when iodide is replaced with bromide. The functional dependence of the band gap with respect to the bromide content seems to be independent of the MA/FA-ratio. The difference in band gap between a pure iodide perovskite and a pure bromide perovskite is approximately 0.7 eV, which is highly desirable for the design of tandem architectures. The increase in band gap with increasing bromide content is non-linear. Given the limited amount of data points and the resolution of the measurements, a quadratic expression gives a good agreement with the experimental data.

The exchange of the organic ion has a rather small effect on the band gap. This is consistent with the calculated PDOS curves showing that the organic ions provide negligible density of states close to the band edges. A small decrease in the order of a few tenths of an eV can, however, be seen when MA is replaced by FA. The reason for this shift is most likely an indirect steric effect as the different size of the ions will lead to different tilting angles between the lead-halogen octahedra, which have been demonstrated to effect the band gap[60-63].

In order to numerically describe the dependence of band gap with respect to the perovskite composition in the MA/FA/Br/I compositional space, an empirical relation was fitted to the experimental data. The band gap is assumed to depend linearly on the FA/MA-ratio and quadratic on the Br/I-composition. There is no deep physical argument behind the chosen functional form other than that a linear relation obviously is wrong, that a second order polynomial gives an adequate fit to the experimental data, and that the data is too scarce to give a physical meaning to a relation with additional free parameters. The samples in the pure FA series were excluded from the analysis as XRD measurements shows that the intended perovskite were not the dominant phase for all of those samples (2,3). The relation is given in eqn. 1. Confidence interval of the determined coefficients can be found in the supporting information.

$$Eg(x,y) = 1.58 + 0.436x - 0.0580y + 0.294x^2 + 0.0199x \cdot y$$
$$x = \frac{[Br]}{[Br]+[I]}, y = \frac{[FA]}{[FA]+[MA]} \quad (1)$$

A part of the interest of the mixed perovskites is the ability to tune the band gap in order to get a good match between the two photoabsorbers in a tandem architecture where the perovskite is used as a top cell. While evaluating the expectations that could be set upon an efficient tandem system, a good limiting case is the optical limit of the current density under ideal conditions. The theoretical maximum current achivable from a two band gap tandem system, given as a function of the band gap of the top and bottom cells under AM 1.5 illumination, is given in figure 5.a. Some of the most relevant vertical paths in figure 5.a are given in figure 5.b where the optical limit of the photocurrent is plotted as a function of the band gap for the top cell, which could be a perovskite, against the band gap of some possible bottom cells. The details of these calculations are given in the supporting information. It is apparent that the efficiency that could be obtained by the tandem system, with a given bottom cell, drops rather fast when the band gap of the top cell deviates from the ideal match. This is entirely symmetrical for the band gap of the bottom cell if the band gap of the top cell is fixed. This analysis clearly illustrates the importance of being able to tune at least one of the band gaps while designing tandem cells, as is the case for the perovskites. More important than the current is the output power, which depends on a fairly long range of parameters. If reasonable parameters are chosen, an estimation of what can be obtained from a good tandem device is given in figure 5.c. Based on those theoretical estimations, the band gaps derived from eqn. 1 were used to predict where in the compositional space, illustrated in figure 1, the ideal band gaps would be found for making top cells together with bottom cells of different band gaps. That estimation is illustrated in figure 4.c for band gaps corresponding to the commercially available solar cell technologies that could be interesting for tandem application together with perovskites. To get a band gap that would match silicon, a bromide content of around 30 % is required, whereas for a GaAs bottom cell a bromide content of around 60 % would be needed. For a perovskite/perovskite tandem cell, even higher bromide contents would be necessary for the top cell.

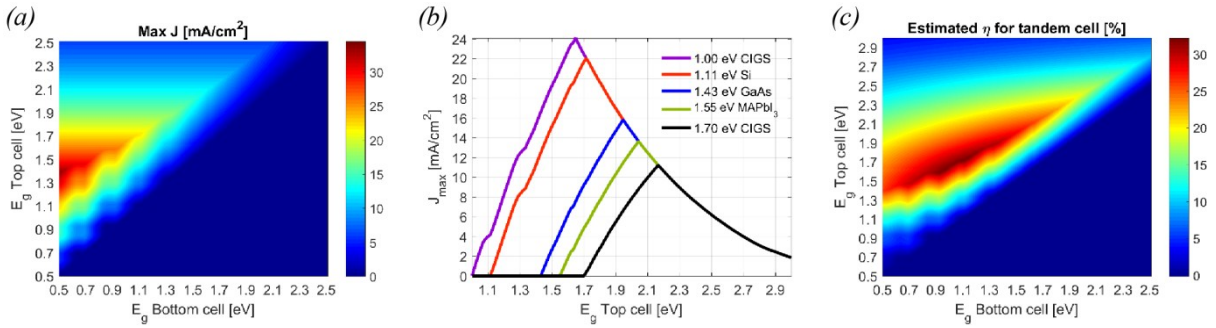

Figure 5. (a) Ideal optical limit current limit in a tandem cell as a function of the band gaps of the top and bottom cell. (b) Optical current limit for a tandem cell as a function of the band gap of the top cell for a number of possible bottom cells. (c) Estimated top performance of a tandem cell as a function of the band gap for the top and bottom cells. The details of the calculations are presented in the supporting information

Steady state photoluminescence

Steady state photoluminescence was measured on perovskite films deposited on both soda lime glass, SLG, with a 15 nm thick amorphous SnO_2 layer, and on substrates with mesoporous TiO_2. No significant difference was observed with respect to the substrate, but the PL-intensity was on average somewhat higher for the films deposited on SLG, for which we present data below. In figure 6.a-c, PL-spectra, together with absorption data, are given for three representative samples that illustrate the main type of observed PL-behavior. The corresponding figures for all compositions are found in the supporting information.

For samples with no bromide, or only a small fraction of bromide, one distinct PL-peak centered on energies slightly higher than the band gap energy is observed, as illustrated in figure 6.a. This would correspond to direct recombination from the conduction band edge to the valence band edge. For the pure bromide perovskites without iodide, one PL-peak centered on the band gap energy is observed, as in figure 6.c. Those peaks are narrower than for the pure iodine perovskites, conforming to the more excitonic nature of the absorption for the bromide perovskites observed in the absorption data analyzed in the previous section. For films with 50 % bromide or more, excluding the pure bromide perovskites, the photoluminescence behavior is distinctly different and more than one peak is observed in the PL-spectra, as illustrated in figure 6.b. The peak at higher energy corresponds to the band edge recombination in the dominant phase, but there is also one peak at lower photon energies.

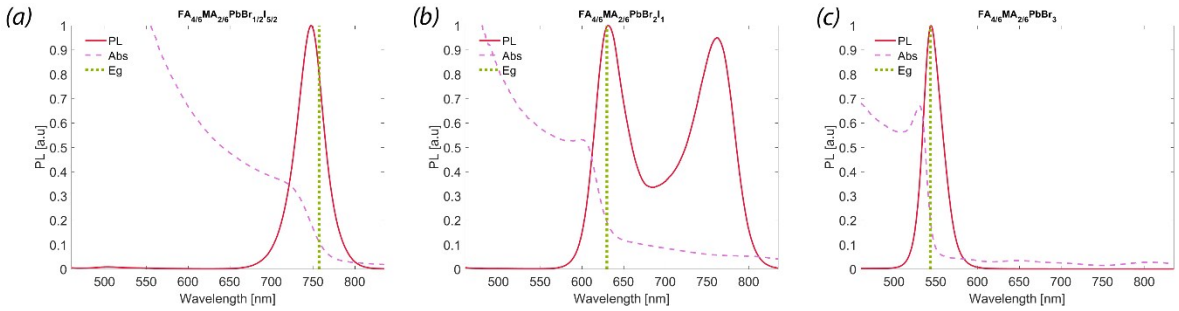

Figure 6. Normalized photoluminescese and optical absorption for representative samples: (a) Sample 16, $FA_{4/6}MA_{2/6}PbBr_{1/2}I_{5/2}$ (b) Sample 19, $FA_{4/6}MA_{2/6}PbBr_2I$ and (c) sample 21 $FA_{4/6}MA_{2/6}PbBr_3$. The band gap energy is illustrated by a vertical line in the figures.

From the point in the compositional space where two PL-peaks start to be observed and towards higher bromide contents, the relative intensity of the emission at lower energies increases compared to the intensity for the band edge recombination. One possible explanation for this would be that these perovskites have more trap states within the band gap that can act as recombination centers. The nature of those traps is still unclear and should be considered in future investigations. Another explanation would be a phase separation with the formation of small amounts of a minority phase. That secondary phase would be an iodide rich perovskite phase with a lower band gap. The photo-excited charge carriers could easily be trapped in this secondary phase, as illustrated in figure 7a-c. Once the charge carriers get trapped in this phase, radiative recombination within the minority phase is a likely outcome. The relative amount of emission from the minority phase increases when the bromide content increases, indicating either more of the minority phase, or that the charge carriers are more easily or deeply trapped. Given the gradual shift in energy of the band gap emission with respect to the perovskite composition, it is reasonable to assume that the majority phase is a true mixed perovskite. The emission energy for the secondary phase indicates that it is an iodide rich phase and the emission energies for this phase is in a similar energy range for all the samples with this behavior, regardless of the overall composition. The difference in band gap between the minority and the majority phase thus increases as the overall bromide composition increases. The charge carriers trapped by the minority phase would thus be more deeply trapped, and have a lower probability for escape when the bromide concentration increases. This is in line with the stronger relative intensity for the trap induced emission for the more bromide rich compounds.

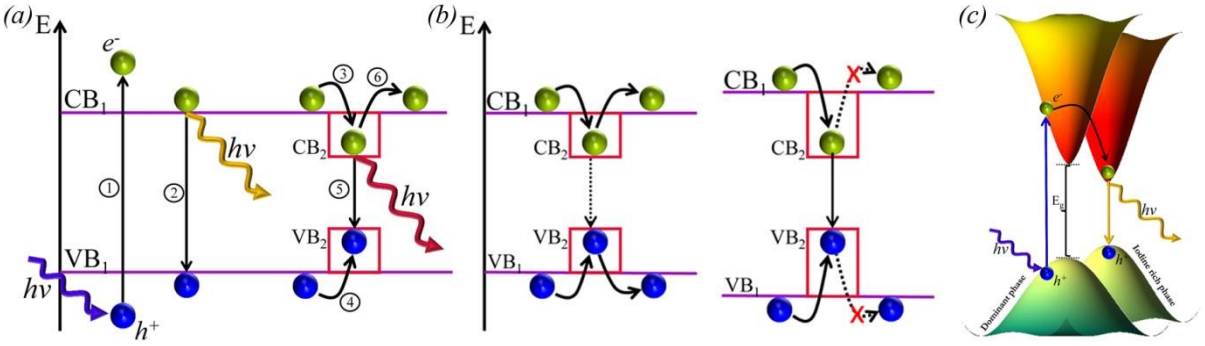

Figure 7. (a) Illustration of trap assisted recombination by an iodide rich minority phase. The different processes are: (1) Absorption, (2) Band edge recombination, (3) Trapping of electrons by minority phase, (4) Trapping of hole by minority phase, (5) Radiative recombination by the minority phase, de-trapping of the electron. (b) Illustration of the increased importance of trapping as the band gap difference between the minority and the majority phase increases. (c) A three dimensional illustration of electron transfer from the majority to the minority phase. The cones are representative of the density of states at the conduction and valence band edges in the k-space of the perovskite.

This type of phase separation is potentially a problem and the device performance correlates with this behavior. The perovskite compositions with the strongest sub band gap photoemission result in the worst device performance.

This kind of phase separation has been observed before, in for example a study by Friend et. al.[28], in which the MAPb-Br/I system, which corresponds to the bottom most line in figure 1 (sample 42-49), was investigated. They observed a similar PL-behavior, indicating a phase separation, but they also observe the two photoluminescence peaks to merge into one peak after a few weeks. That indicates that given time for diffusion and entropy to play its part, the end result will be one homogeneous phase. We have measured the PL-spectra of the samples after a few days as well as after more than two weeks. We do see a tendency for the minority phase to diminish, but the effect is not at all as clear as in the work of Friend et. al.[28]. For most samples in the matrix, the behavior is qualitatively the same after a few days and after more than two weeks. This indicates that this sub band gap recombination may be a persistent problem for the bromide rich perovskites.

A variation of this behavior has also been observed by Hoke et. al.[26], which investigated the MAPb-Br/I system as well. They found that under one sun illumination, a phase segregation occurs, resulting in the same split of the PL-emission as observed in the present work. They found it to occur within the time frame of a minute, and that the behavior was fully reversible. That is, however, probably not the cause behind the observations in this study. The PL-measurements take several minutes which is longer than the time frames under which they observe the onset of phase segregation to occur, but the illumination is also considerably less than one sun. Most convincing is that the PL-splitting here is only observed for certain compositions, whereas Hoke et. al. observes it for all their compositions.

The phase separation hypothesis is, however, undermined by the fact that no support for a secondary phase is found in the XRD data or in the absorption data, which instead indicates one completely dominating phase. That does not exclude the presence of a smaller amount of secondary phase but it shows that if it is there, it is there only to a very small extent. The long diffusion lengths reported in perovskites[64, 65], does however, means that even if inclusions of secondary phases are small and widely apart they may act as efficient recombination centers.

A typical trend in the PL-behavior when the Br/I-ratio is changed is illustrated in figure 8.a. When the amount of bromide is increased, there is a blue shift in the emission peak that mirrors the band gap shift. Overlaid on this trend is the tendency of more than one emission band to occur at higher bromide contents. When the organic ion is changed, the effect on the photoluminescence is much smaller, which is in line with the smaller shift in the bad gap.

This is illustrated in figure 8.b. The PL-peak positions for the primary PL-peak close to the band gap energy are given in table 2. The corresponding peak positions for the secondary peak found for the bromide rich samples are found in the supporting information.

The total emission intensity varies broadly over the different compositions. The peak intensity as a function of composition is given in figure 8.c. The highest emissions are found for the pure bromide perovskites and the lowest for the pure iodine perovskites. Intermediate intensities are found for the formamidinium rich perovskites with a small amount of bromide, and for the methyl ammonium rich perovskites with plenty of bromide. The rather high PL-emission for the FA and Br rich perovskites correlates with high device performance and could simply be an indication of high crystal quality. For the bromide rich perovskites, it is more likely a consequence of the assumed secondary phase which acts as radiative recombination centers. The highest PL-intensities are, however, found for the pure bromide perovskites. That could indicate a high crystal quality but it could also be a consequence of the higher exciton energy observed in the absorption measurements.

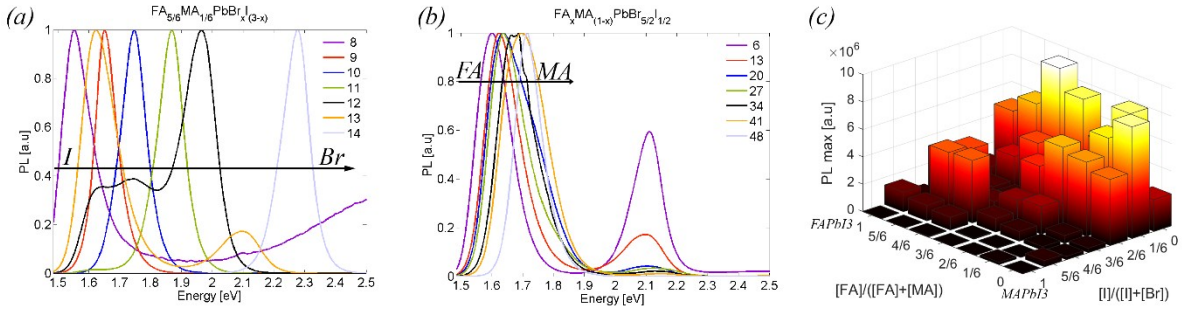

Figure 8. (a) Normalized PL spectra while the iodine/bromide ratio is changed. (b) Normalized PL spectra while the FA/MA ratio is changed. (c) Maximum emission intensity as a function of composition.

Table 2. Primary PL Peak position [eV]

Pb	I_3	$Br_{0.5}I_{2.5}$	Br_1I_2	$Br_{1.5}I_{1.5}$	Br_2I_1	$Br_{2.5}I_{0.5}$	Br_3
FA	1.56	1.64	1.76	1.87	1.96	2.11	2.28
$FA_{5/6}MA_{1/6}$	1.55	1.65	1.75	1.87	1.97	2.10	2.28
$FA_{4/6}MA_{2/6}$	1.56	1.66	1.70	1.86	1.97	2.11	2.28
$FA_{3/6}MA_{3/6}$	1.59	1.65	1.77	1.85	1.88	2.12	2.28
$FA_{2/6}MA_{4/6}$	1.62	1.65	1.77	1.83	1.94	2.13	2.29
$FA_{1/6}MA_{5/6}$	1.64	1.60	1.77	1.85	1.95	2.15	2.30
MA	1.61	1.68	1.71	1.85	1.70	1.72	2.30

Surface morphology

To evaluate the surface morphology, top view images were taken by a scanning electron microscope (SEM) of the perovskite films. SEM images for all the compositions are given in figure 9. Images at both higher and lower magnifications are available in the supporting information. There are certainly differences in morphology between the samples. Some compositions appear to have larger grains, and others appear to have a rougher surface. For device performance, these are important factors that are known to have a significant impact on the final solar cell device. The main conclusion that can be drawn from these data is, however, that the surface morphology is surprisingly similar for the different compositions; especially while compared to the vast diversity of surface morphologies that are found in the literature for $MAPbI_3$ alone. For all compositions, compact and fairly smooth films are formed, and the number of pinholes is small for all compositions. The grain size differs a bit but no clear major trends have been found, even though it appears to be distinctly larger for the two unmixed bromide compositions. One trend that is observed is that films with higher bromide content are a bit smoother, which correlate with the smaller amount of light scattering seen in

figure 3.c. The bromide rich films are also more strongly affected by the electron beam and while they are observed, cracks open up between the grains which is seen in some of the figures. That is not observed for the more iodide rich perovskites. That could indicate more fragile grain boundaries, which potentially could lead to a problem of charge carrier transport through or along the grain boundaries.

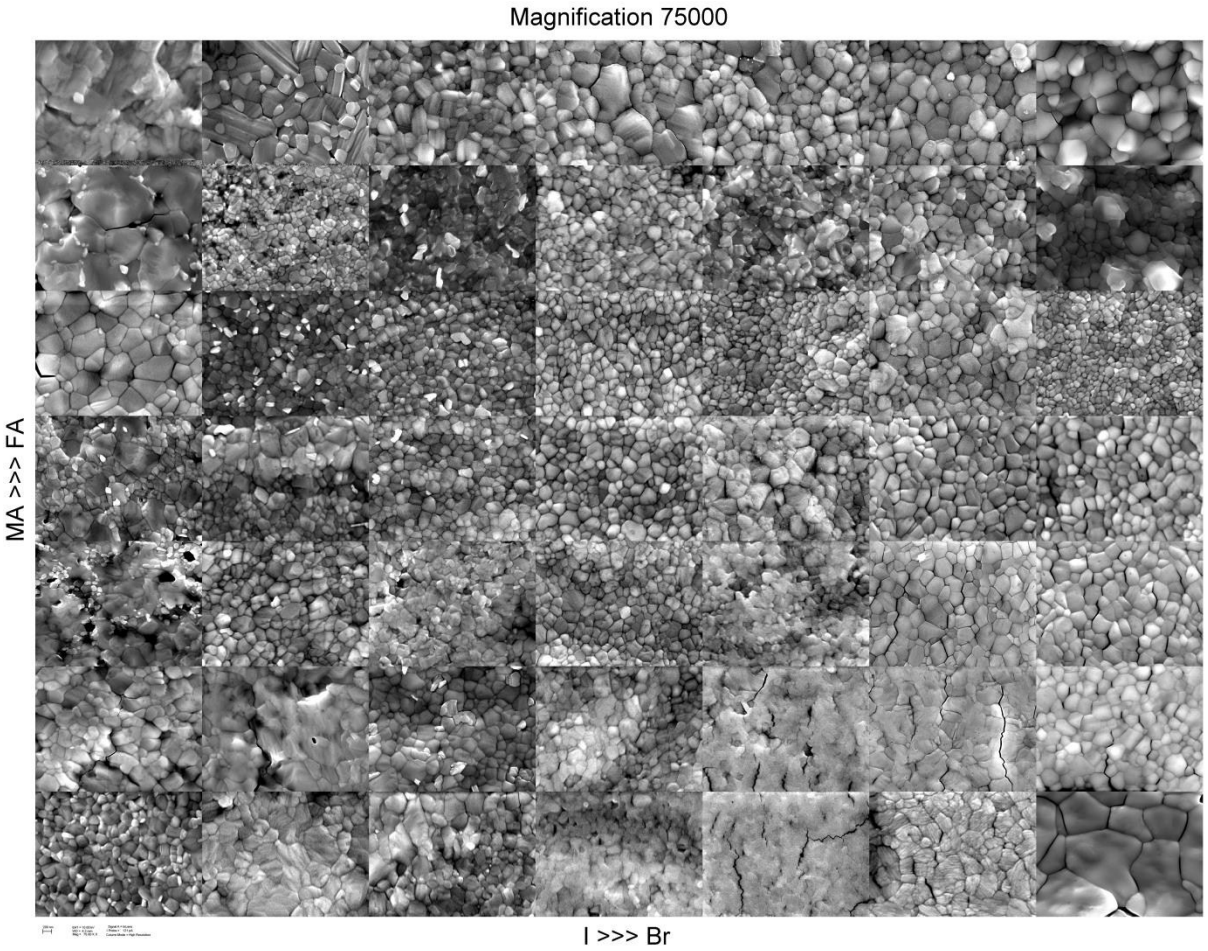

Figure 9. SEM images of the films of different composition. The panels are in the same order as in the samples in figure 1. The width of each sub-panel is 3.9 µm. The composition for the best device corresponds to the panel that is the second from the left in the third row from the top.

The best solar cell device were made from composition 16, which corresponds to the panel that is the second from the left in the third row from the top in figure 9. The surface morphology of that film does not stand out from the other nearby compositions in any significant way. The employed preparation procedure thus gives surface morphologies that are fairly similar for the different compositions. They are similar enough for it to be reasonable to assume that most of the differences in physical properties observed over the compositional space in this study indeed have their origin in the physics of the perovskites rather than being effects related to surface morphologies.

Crystallographic properties

X-ray diffraction, XRD, was measured for all 49 compositions. An example of a diffractogram is given in figure 10.a where data for $FA_{4/6}MA_{2/6}PbBr_{1/2}I_{5/2}$, which provided the highest device efficiency, is given. That diffractogram is qualitatively representative for most of the compositions. The full set of diffractograms is found in the supporting information.

The iodine rich pure FA-samples (2 and 3) deviate from the others and the dominating phase is not the photoactive perovskite. Also the $FAPbI_3$-sample has peaks that do not com from the perovskite phase. For these samples, the hexagonal, yellow $FAPbI_3$ polymorph[11,54] formed instead. This is in line with the absorption data that deviates for these samples as well. Disregarding these three compositions in the upper left corner of the composition space, the intended perovskite formed and was the dominant phase in all samples. That phase is also present in compositions 1-3 but not as the most prominent one. In two other compositions (27 and 38), a few peaks are observed that cannot be explained by the perovskite phase. Apart from these deviations, the only crystalline phases detected are the intended perovskites, PbI_2, and $PbBr_2$. The PL-measurements indicate a phase separation in the bromide rich samples, but the XRD-data does not support that hypothesis. If there is a secondary perovskite phase in the bromide rich perovskites, it is either amorphous or present in an amount smaller than we managed to detect.

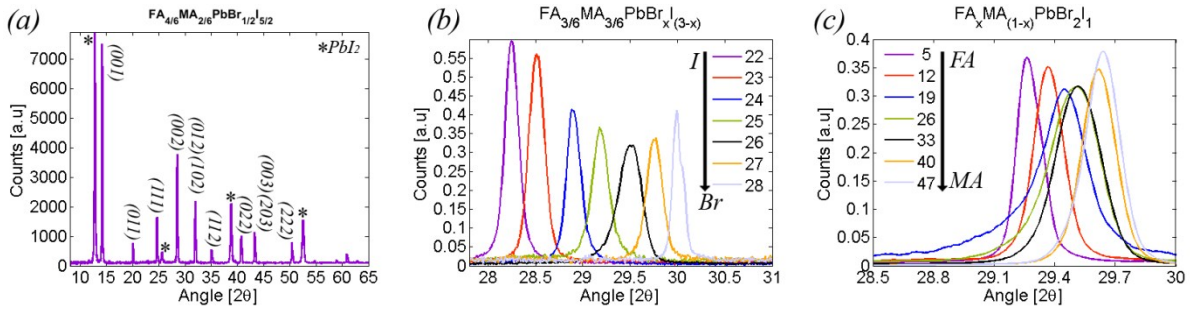

Figure 10. (a) XRD data for composition 16, $FA_{4/6}MA_{2/6}PbBr_{1/2}I_{5/2}$. (b) The (002) peak as a function of bromide content. (c) The (002) peak as a function of FA content. In (b) and (c), data is scaled with the intensity of the (001) peak.

As iodide ion is larger than the bromide ion, the unit cell is expected to contract if iodide is replaced by bromide. In line with Bragg's law, a smaller d-spacing shift the diffraction peaks to larger diffraction angles. That is also observed, as illustrated for the (002) reflex in figure 10.b. In the same way the diffraction peaks shift to smaller diffraction angles when MA is replaced with the larger FA-ion, as illustrated in figure 10.c. The effect is, however, considerably smaller than when the halogen is exchanged. Figures illustrating these peak-shifts for all subset of samples are found in the supporting information.

In figure 10.b, the diffraction peaks are somewhat broader for the more bromide rich samples, excluding the pure bromide perovskites. That indicate slightly smaller crystallites, which potentially could be bad for the device performance[66], but this is likely not a main cause for the lower device performance seen for these compositions.

Perovskites are found with a few different crystal symmetries, as described by the tolerance factor, *t*, introduced by Goldschmidt in the 1920's[67]. The tolerance factor relates the structure of an ABC_3 perovskite to the ionic radiuses according to eqn. 2, where r_A, r_B, r_C, are the ionic radius of the *A*, *B*, and *C* ions, respectively.

$$t = \frac{r_A + r_C}{\sqrt{2}(r_B + r_C)} \qquad (2)$$

For a tolerance factor between 0.9 and 1, a cubic structure is preferred at room temperature, whereas for values of *t* between 0.7 and 0.9, orthorhombic, rhombohedral or tetragonal structures are favoured. Perovskites with a tetragonal structure at room temperature tend to transform into a cubic phase at higher temperatures. For $MAPbI_3$, this occurs around 54ºC[68], which is in the operational window of a solar cell. A perovskite with a cubic structure at room temperature could potentially be advantageous as that phase transformation then is avoided.

The ionic radius is 0.132 nm for Pb^{2+}, 0.206 nm for I^- and 0.18 nm for $CH_3NH_3^+$ [69]. That gives a tolerance factor of 0.81 for $MAPbI_3$, which is consistent with the tetragonal structure found experimentally[70, 71]. The bromide ion is slightly smaller (0.182 nm) than the iodide ion, but the tolerance factor is only increased to 0.82. Based on the similarity of the tolerance factors, it would be reasonable to assume a tetragonal crystal structure also for $MAPbBr_3$. That is also in line with our data, but single crystal data for $MAPbBr_3$ indicate that a cubic structure is formed[71-73].

The formamidinium ion is slightly larger than the methyl ammonium ion which will increase the tolerance factor, favouring a cubic structure for the formamidiumium rich compositions. $FAPbI_3$ is also found in a cubic perovskite phase[74] or a singly distorted pseudo-cubic trigonal phase[14, 75] but has also been reported to form a tetragonal structure[29, 76]. A problem with $FAPbI_3$ is the instability of the perovskite phase which is not thermodynamically stable at room temperature and a transformation into a hexagonal yellow polymorph is frequently observed[14, 77]. Less work have been conducted on $FAPbBr_3$ but it has been reported to form a cubic phase at room temperature[54].

To facilitate the interpretation of the experimental XRD-data, theoretical powder diffractograms based on experimental single crystal data were simulated for both the cubic and a tetragonal phase of $MAPbI_3$. Those are displayed and further discussed in the supporting information. The difference between the tetragonal and the cubic structure is seen as a few extra peaks for the tetragonal phase, like the (121) peak, and a split of some peaks seen as single peaks in the cubic structure. This differences were elaborated in some detail in one of our previous publications[68]. The differences are, however, not very large and for polycrystalline films, good XRD-data of samples without too strong texture is required in order to assess the crystal phase with accuracy.

For composition 1 to 38 (FA rich devices), the experimental XRD-data is in line with a cubic structure. Essentially all of the expected diffraction peaks occur in these diffractograms which both indicate a rather random ordering of the crystal grains within the films, and helps in determining the crystal symmetry.

The few XRD-results for $FAPbBr_3$ presented so far indicate the room temperature structure to be cubic[29, 54] which is in line with our data. The perovskite phase of $FAPbI_3$ have been reported to be cubic[74], trigonal phase[14, 75] as well as tetragonal[29, 76]. In a work of Epron et. al[29] a transition between a tetragonal phase was found while going from $FAPbI_3$ to $FAPbBr_3$. The cubic and the trigonal phases are close and not trivial to separate and while keeping this in mind, the data presented here clearly indicate that all the FA-rich perovksites form a cubic crystal structure at room temperature.

For the pure MA-perovskites and the bromide rich perovskites with 1/6 MA (sample 39 to 49), the diffractograms have a different appearance. A few diffraction peaks dominate the signal which indicate a high degree of texture. This texturing makes it harder to distinguish between a tetragonal and a cubic phase. From before, we know $MAPbI_3$ to crystallize in a tetragonal structure and we know that spin-coating tend to give highly textured films for $MAPbI_3$[68]. This is an indication, but not conclusive evidence, that the transition line between room temperature tetragonal and cubic structures is found around $FA_{1/6}MA_{5/6}PbBr_1I_2$ (sample 38). That is in agreement with Goldsmiths tolerance factor in eqn. 2 that predicts $MAPbI_3$ and $MAPbBr_3$ to have the same crystal structure. It is, however, a weak conclusion as several

groups have found $MAPbBr_3$ in a cubic structure[71-73]. This will require further investigations but clear is that spin-coated films of $MAPbBr_3$ crystallographically appears to have more in common with the tetragonal $MAPbI_3$ than with the cubic $MAPbBr_3$.

Given the diffraction angles, Bragg's law, the indexation given in figure 10.a, and the relation between cell parameters and the d-spacing in a given crystal symmetry, the cell parameters were determined. These are given in the supporting information. The corresponding cell volume is given in table 3, where it can be seen that changing the organic ion has a smaller impact on the cell volume than changing the halogen, which has a relatively larger effect. The cell volume of $FAPbI_3$ is 22 % larger than that of $MAPbBr_3$.

Table 3. Volume of the primitive unit cell expressed in $Å^3$.

Pb	I_3	$Br_{0.5}I_{2.5}$	Br_1I_2	$Br_{1.5}I_{1.5}$	$Br_2I_{1.}$	$Br_{2.5}I_{0.5}$	Br_3
FA	255	242	240	230	225	222	215
$FA_{5/6}MA_{1/6}$	255	248	233	227	221	219	213
$FA_{4/6}MA_{2/6}$	254	247	243	226	220	216	211
$FA_{3/6}MA_{3/6}$	253	246	237	226	221	216	210
$FA_{2/6}MA_{4/6}$	252	243	236	225	221	217	210
$FA_{1/6}MA_{5/6}$	244	249	235	220	218	216	209
MA	248	241	234	227	221	221	209

A rather interesting result extracted from the XRD data is a difference in the tendency for the two lead salts, PbI_2 and $PbBr_2$, to form the perovskites. Recent reports have demonstrated that an excess of PbI_2 in the precursor solutions, which will leave unreacted PbI_2 within the perovskite films, is beneficial for device performance[42-44]. A 10 % excess of lead salts, with respect to the organic halogens, was therefore used in all precursor solutions. This is expected to result in some unreacted PbI_2 and $PbBr_2$ in the films, which should be detected by XRD. Interestingly, $PbBr_2$ is only observed in the pure Br-compositions where no PbI_2 is present in the precursor solutions. As soon as both PbI_2 and $PbBr_2$ are present in the precursor solution, PbI_2, but not $PbBr_2$ is observed in the XRD diffractogram. That means that $PbBr_2$ participates in the perovskite formation more easily than PbI_2. This is an insight that could be valuable in the further understanding of the crystallization process for the mixed perovskites, and in the end also contributes to the understanding of the role played by the PbI_2-excess currently debated in the literature. The reason behind this behavior could possibly be attributed to the different crystal structures of PbI_2 and $PbBr_2$. PbI_2 has a layered structure with layers composed of edge sharing PbI_6 octahedra, whereas $PbBr_2$ form an interlinked network of edge and corner sharing $PbBr_6$ octahedra. This difference in crystal structure between the two lead salts will most likely be of importance for the formation mechanisms of the perovskites, which briefly is elaborated in the supporting information.

Device performance

An illustration of how our solar cell devices look like and how they are built is shown in figure 11.a-c. Full solar cell devices were made with all 49 different compositions, and the results are summarized in figure 12.a-d, and in table 4. The device performance shows a huge spread within this compositional matrix and the efficiencies vary from 2.3% to 20.7 %.

Making an efficient device is tricky, involves a fair bit of artisanship, and is affected by a number of environmental parameters that are challenging to control and at the moment not well understood. This is the reason for both a cell to cell and a batch to batch variation of device performance observed by many groups in the field. That means that data for device performance has a larger standard deviation as compared to the XRD, absorption, and photoluminescence measurements discussed above. Nevertheless, device performance is a key measure for assessing the potential impact of perovskite solar cells for the industry, and there

is a wealth of interesting information that could be found in the device measurements performed; especially when the trends are as clear as they are in the current dataset.

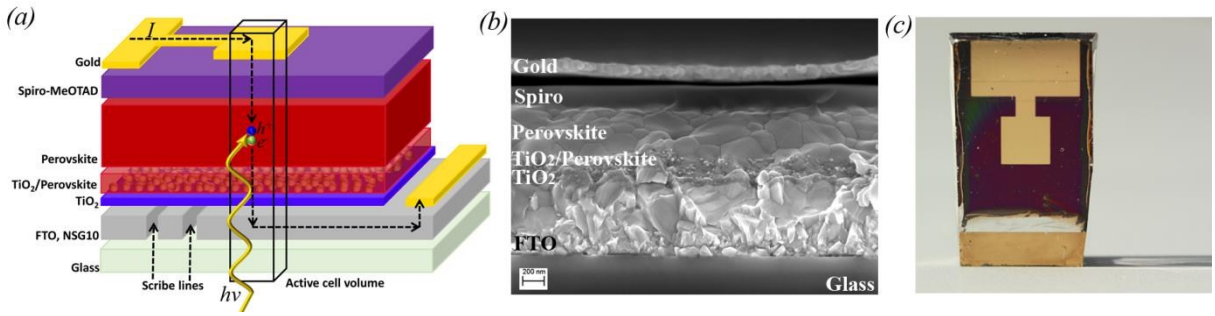

Figure 11. (a) A schematic cross section of the device architecture used. (b) A cross section of one of the highest performing cells. The scale bar is 200 nm. (c) A photo of one of the devices.

Of the 49 compositions, $MA_{2/6}FA_{4/6}Pb(Br_{1/6}I_{5/6})_3$ (sample 16), yielded the best devices, with a top efficiency of 20.67%, as illustrated in figure 12 and 13.a. In subsequent experiments, this composition has turned out to consistently give high efficiency devices. Most of the best devices reported so far are also based on the MA/FA/Br/I mixed perovskites, but with a slightly different composition[17, 31, 32].

There is always some uncertainty associated with efficiency numbers due to the challenges in measure them correctly. The results for high efficiency devices measured with the current IV-setup have recently been shown to agree well with results measured by independent testing facilities, which give credibility to this high efficiency. This is truly a state-of-the-art device, and at the moment of testing the performance was distinctly better than the certified record in NREL's solar cell efficiency chart which at that time was 20.1% coming from the group of Seok[17]. At the time of submission, the highest certified cell efficiency had very recently reached 21.02 %, measured on a cell from our laboratory based on the mixed perovskites discussed in this work.

The best cells have compositions clustered around $MA_{2/6}FA_{4/6}Pb(Br_{1/6}I_{5/6})_3$ (sample 16), where a part of the iodide is replaced by bromide and where most of the MA is replaced by FA. Increasing the bromide content further decreases the cell performance and the worst results were obtained where almost all of the iodide was replaced with bromide. For the pure bromide devices, the efficiencies go up again and reaches around 7 % for the best cells. That is in line with the best bromide devices published[54] that also reach around 7%. Slightly higher open circuit voltages, V_{oc}, has been observed (1.5 V) but with a significantly lower efficiency[78]. Also the pure bromide devices here presented are thus good representatives of the current state-of-the-art.

The V_{oc} are around 1.15 V for compositions around $MA_{2/6}FA_{4/6}Pb(Br_{1/6}I_{5/6})_3$ (sample 16). While the bromide content is increased, the band gap is increased and an increase in V_{oc} could therefore be expected. The reverse trend is, however, observed. The decrease in V_{oc} correlates with the PL-behavior which indicates that a larger fraction of bromide introduces efficient recombination centers within the band gap, which possibly could be related to a phase separation. For the pure bromide devices, the V_{oc} increases again and the highest V_{oc} is found for those devices. With respect to the band gap of approximately 2.3 eV, a V_{oc} of 1.4 V is, however, not particularly noteworthy and there is a large potential for improvements. For the pure iodine perovskites, the V_{oc} is around 1 V or below which is lower than what have been reported before. That could be related to the low PL-intensity for those compositions, which indicate that something in the synthesis procedure not carried over favorably to these compositions.

The short circuit current is also highest around $MA_{2/6}FA_{4/6}Pb(Br_{1/6}I_{5/6})_3$ (sample16). For higher bromide compositions, the current is expected to decrease as the band gap increases. The photocurrent does indeed decrease but the observed drop is considerably larger than what could be expected based on the absorption and is probably a result of the sub band gap recombination seen in the PL-measurements. The fill factor shows a similar functional dependence on the composition as the overall efficiency. In figure 16.d, the fill factor appears to be over unity for some of the compositions in the lower right corner (close to $MAPbBr_3$). That does not represent true fill factors but is a mathematical artifact resulting from strong hysteresis in those devices.

The external quantum efficiency, *EQE*, has been measured as a function of wavelength and in figure 13.b, this is illustrated for a series of samples where iodide gradually is replaced by bromide. The *EQE* data does not provide any unexpected information and follows well the absorption and PL-data.

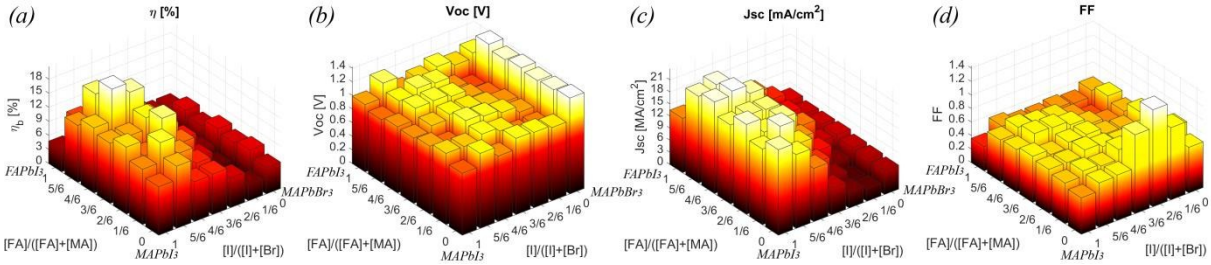

Figure 12. Device parameters for cells of different composition. (a) η. (b) Voc. (c) Jsc. (d) FF.

Table 4. Key parameters for the device performance for each of the 49 compositions investigated. The positions in the tables correspond to the compositions outlined in figure 1. The data refer to the reversed scan direction

	η [%]							J_{sc} [mA/cm²]						
Pb	I_3	$Br_{0.5}I_{2.5}$	Br_1I_2	$Br_{1.5}I_{1.5}$	$Br_2I_{1.}$	$Br_{2.5}I_{0.5}$	Br_3	I_3	$Br_{0.5}I_{2.5}$	Br_1I_2	$Br_{1.5}I_{1.5}$	$Br_2I_{1.}$	$Br_{2.5}I_{0.5}$	Br_3
FA	4.8	9.6	1.9	3.7	7.5	5.0	5.0	13.5	14.3	3.9	7.1	12.8	9.7	7.5
$FA_{5/6}MA_{1/6}$	12.1	17.4	14.7	11.4	5.8	3.3	6.5	21.5	22.7	19.1	15.6	11.1	8.8	7.0
$FA_{4/6}MA_{2/6}$	13.9	20.7	18.5	11.7	5.6	3.4	5.5	22.7	23.7	21.4	15.3	9.5	7.2	7.0
$FA_{3/6}MA_{3/6}$	12.8	12.9	15.3	11.9	7.9	3.9	7.1	19.6	20.4	20.0	15.5	12.6	6.9	7.0
$FA_{2/6}MA_{4/6}$	14.3	11.0	17.5	10.7	6.2	2.9	6.4	22.3	18.7	20.4	13.9	9.0	4.4	6.4
$FA_{1/6}MA_{5/6}$	11.8	16.0	12.2	8.7	3.5	2.3	7.1	18.8	22.7	16.7	10.3	5.1	2.8	6.3
MA	10.3	13.2	8.5	8.6	6.3	3.5	5.6	21.2	18.3	13.2	6.6	4.0	3.0	5.9

	V_{oc} [V]							FF						
Pb	I_3	$Br_{0.5}I_{2.5}$	Br_1I_2	$Br_{1.5}I_{1.5}$	$Br_2I_{1.}$	$Br_{2.5}I_{0.5}$	Br_3	I_3	$Br_{0.5}I_{2.5}$	Br_1I_2	$Br_{1.5}I_{1.5}$	$Br_2I_{1.}$	$Br_{2.5}I_{0.5}$	Br_3
FA	0.99	1.20	0.99	1.06	1.14	1.06	1.14	0.36	0.56	0.50	0.50	0.52	0.49	0.58
$FA_{5/6}MA_{1/6}$	0.92	1.10	1.18	1.15	0.98	0.88	1.42	0.61	0.70	0.65	0.63	0.54	0.43	0.65
$FA_{4/6}MA_{2/6}$	0.97	1.14	1.15	1.11	1.00	0.92	1.35	0.63	0.76	0.75	0.69	0.59	0.51	0.58
$FA_{3/6}MA_{3/6}$	0.96	1.04	1.10	1.09	1.03	0.98	1.39	0.68	0.61	0.69	0.70	0.60	0.58	0.73
$FA_{2/6}MA_{4/6}$	1.00	0.91	1.17	1.13	1.08	0.99	1.35	0.65	0.64	0.73	0.68	0.64	0.66	0.72
$FA_{1/6}MA_{5/6}$	1.05	1.04	1.12	1.07	0.94	0.95	1.37	0.60	0.68	0.65	0.79	0.74	0.86	0.81
MA	0.91	1.10	0.96	1.12	1.10	1.07	1.41	0.54	0.66	0.67	1.17	1.43	1.07	0.67

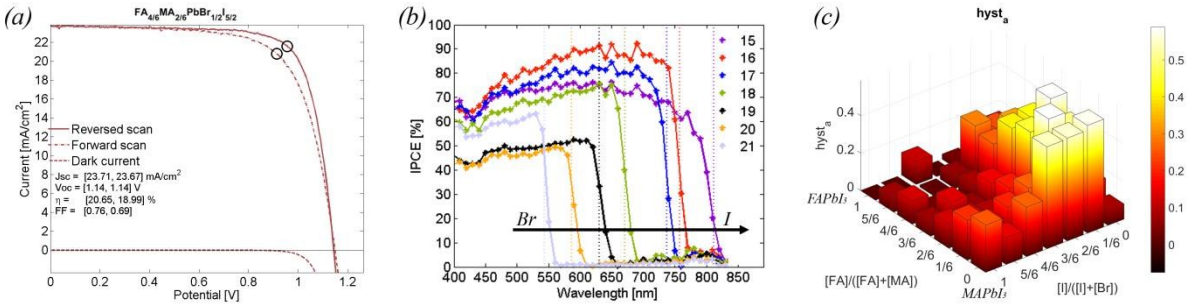

Figure 13. (a) IV data for the best device. The full set of IV-curves is found in the supporting information (b) EQE data for a few devices with different bromide content. (c) Hysteresis according to eqn. 3 given as a function of composition.

Hysteresis in the current-voltage dynamics for the perovskite cells has been widely observed and discussed for the perovskite cells[79-82]. There are several hypothesizes concerning the origin of the hysteresis involving ion migration[83], interfacial charge transfer[84], capacitive effects[80], and ferroelectric effects[85]. Hysteresis could, depending on the underlying mechanism, be a problem for the long term device performance, and it is definitely a potential problem while evaluating device performance[86]. It could also be viewed as a window into the physics of the system and as a tool for gaining a deeper understanding. A measure of the degree of hysteresis is given by eqn. 3, which defines the hysteresis, *H*, as the fraction of the difference between the area swept by the current in the backwards and forwards scan, J_f and J_b, with the area swept by the current of the backwards scan. There are a number of other measures of the hysteresis proposed in the literature which instead of computing the difference in the integrated current simply evaluate the current at specified values of the voltage[79, 80], but they do not capture the hysteresis dynamics to the same extent as the definition in eqn. 3.

$$H = \frac{\int_0^{V_{oc}} J_b(V)dV - \int_0^{V_{oc}} J_f(V)dV}{\int_0^{V_{oc}} J_b(V)dV} \qquad (3)$$

The hysteresis as a function of cell composition is given in figure 13.c. It is fairly small for devices with a high fraction of both iodide and FA, and is higher for bromide and MA rich devices. At this instance, we cannot give conclusive evidence for a mechanism that would completely explain the observed hysteresis behavior, but there are some hypotheses that reasonably well conforms to the data.

As an aid in these speculations, and to predict the trend in the bandgap shifts in the mixed perovskites, periodic crystal calculations of the four corner compounds: $MAPbI_3$, $MAPbBr_3$, $FAPbI_3$, and $FAPbBr_3$ were performed. From these calculations, the band gaps, the band edge positions, the density of states, DOS, as well as the partial density of states, PDOS, for the metal cation, the halogen, and the organic cation were extracted. The DOS and PDOS-curves are found in the supporting information.

From the simulations, the band gaps of $MAPbI_3$, $MAPbBr_3$, $FAPbI_3$, and $FAPbBr_3$ were determined to 1.6, 2.3, 1.5 and 2.05 eV, respectively. These values are reasonably close to our experimental values, despite the well-known band gap problem associated with DFT-calculations. This indicates that the error cancelation from the spin-orbit coupling and the scalar relativistic effects in lead is favorable in this case[52, 87], rendering a reasonable trustworthiness for qualitative discussions based on the simulated data.

Also the absolute energetic positions of the band edges are important parameters for the operation of photo-absorbers[57, 88]. Those were here qualitatively determined from the DFT-

calculations. The conduction band edge for $FAPbI_3$, $MAPbI_3$, $FAPbBr_3$, and $MAPbBr_3$ were computed to 4.22, 3.9, 4.45 and 3.95 eV, respectively. The corresponding valence band levels were 2.67, 2.3, 2.4 and 1.65 eV, respectively. The exact levels are difficult to pinpoint theoretically due to the nature of the dipolar structure with negatively charge led-halogen octahedra and positively charged dipolar cations, making it hard to obtain trustable ionic bare potential level at infinity[89]. The calculated values are thus not correctly aligned towards the vacuum level, but the trend is in agreement with the tight binding expectations and correlates reasonably well with experimental values found in the literature[75, 90-92]; at least for $FAPbI_3$, $MAPbI_3$, and $MAPbBr_3$. We have not found any experimental data on the band edge positions for $FAPbBr_3$.

The relevant energy levels for these perovskites, based on the simulations, are illustrated in figure 14 in a situation where the perovksite is sandwiched between TiO_2 and spiro-MeOTAD. For the cell to work, the electrons need to be injected from the conduction band of the perovskite into the conduction band of the electron selective contact, and electrons from the valence band in the hole selective contact must be able to inject into the valence band of the perovskite. For this electron transfer to occur, there must to be a driving force, or at least an absence of a barrier. These driving forces are illustrated in figure 14 and can be stated as the energy difference between the conduction band of the perovskite and the electron selective contact, η_{et}, and the difference in energy between the valence band of the perovskite and the hole transporter, η_{ht}. A higher driving force facilitates the charge carrier injection but it has also a negative effect on the photo-voltage.

As the band gap changes while the halogen is replaced, the band edge positions and the driving force for charge carrier transfer will change as well. While iodide is exchanged for bromide, the band gap increases and according to the simulation, this is a combined effect of an upward shift in the conduction band edge and a larger downward shift in the valence band edge. While methyl ammonium is exchanged for formamidinium, there seems to be an upward shift in both the valence and the conduction band. Knowledge of the band edge positions for the corner compounds does not provide knowledge of the situation in the compositional space within the matrix, but a reasonable hypothesis would be that there is a gradual shift with composition. If that hypothesis holds for the entire compositional space, exchanging methyl ammonium to formamidinium could be used as a mean to fine-tune the energy matching between the perovskite and the ETL and HTL with only a small change in the band gap. That would be a useful tool while optimizing device performance.

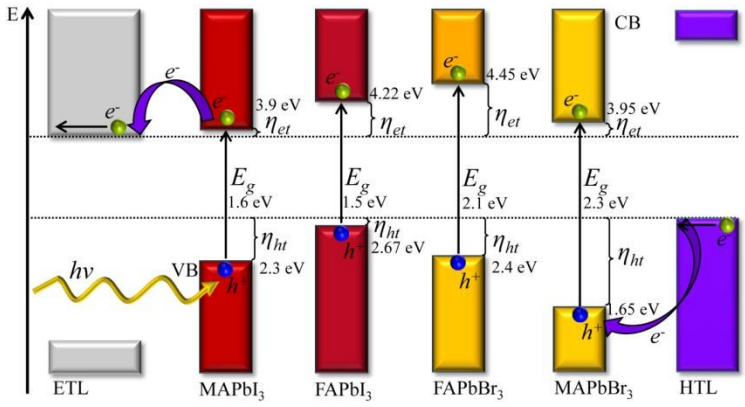

Figure 14. Illustration of band edge matching and the driving force for electron injection between the perovskite, the ETL, and the HTL for different perovskite compositions. The numbers in the figure are from the simulations and are not scaled towards the vacuum level, and thus only relative energy levels are of importance.

As the conduction band edge energies are somewhat lower for the MA-perovskites this would give a decreased driving force for the charge injection into the TiO_2 contact, η_{ht}. This would increase the possibility for charge carrier accumulation at this interface, which potentially could be responsible for the observed increase in hysteresis in the MA-rich perovskites. A way to overcome this could be by more precise surface engineering, which would be more important for the MA-rich perovskites.

Of the ions in the perovskite lattice, the halides are the ones with the lowest activation energy for migration[93]. The bromide rich devices, except the pure bromide devices, shows higher hysteresis with increased bromide content and if the ion migration would be facilitated in those structure, by for example the smaller size of the bromide ion, that could explain part of the trends in the hysteresis. That would, however, need further experimental verification. A more likely hypothesis is instead that trap mediated charge carrier transport are responsible for part of the hysteresis. The PL-data indicate that the bromide rich devices, with the exception of the pure bromide perovskites, have far more traps, which possibly could be due to a phase separation, and that those traps are deeper with higher bromide content. A hysteresis based on successive trapping/de-trapping events would explain one of the major trends in the hysteresis here observed.

One of the strongest conclusions that can be drawn from the device data is that surprisingly small changes in composition can have a large effect in the device performance. In part the difference in performance is due to trap formation in bromide rich perovskites, which is a potential problem for the use of these in tandem devices. In part it could be due to difference in band edge matching to the electron and hole transport layers. In part these differences are probably the result of secondary effects. As was indicated in conjunction to the analysis of the XRD-data, the different crystal structures of PbI_2 and $PbBr_2$ will influence the kinetics and thermodynamics of the perovskite formation process, which will affect crystal quality, grain boundaries, and film morphologies, but these details are still left to be explored.

To some extent, the differences are certainly a consequence of subtle variations in the surface morphology caused by modifications in the crystallization dynamics induced by the difference in composition. The SEM images in figure 9 do, however, indicate that the differences in surface morphology are rather small, especially while compared to the plethora of surface morphologies found in the literature involving: large crystals, small crystals, cuboids, nanorods, smooth films, ruff films, no pinholes, lots of pinholes, etc. This makes it reasonable to ascribe a large part of the difference in device performance to the physics of the perovskite rather than trivial geometrical aspects.

Another way of stating that a small change in composition leads to a large change in device performance is to state that a small change in composition may require a large adaption of the synthesis protocol for the devices to be of similar quality. It is known that different perovskite compositions have different optimized synthesis pathways. That means that the efficiencies here reported for a certain composition by no means represent a limit to what can be achieved by that composition. It is rather a lower limit; a limit that for at least one composition is the state-of-the-art of what have been achieved by perovskite solar cells. An example of the effect of the synthesis protocol is the specific use of solvent. For this experiment, a mixture of DMF and DMSO was used which obviously work very well for the mixed perovskites around $MA_{2/6}FA_{4/6}Pb(Br_{1/6}I_{5/6})_3$. If instead pure DMSO is used as a solvent the efficiencies for the mixed perovskites decreases, but it results in substantially higher efficiencies for the iodine perovskites without any bromide, that then get closer, but not all the way, to the efficiencies here seen for the perovskites around $MA_{2/6}FA_{4/6}Pb(Br_{1/6}I_{5/6})_3$.

The efficiencies for all of the investigated perovskites can thus probably be increased by dedicated optimization work with respect to the synthesis protocol. The data here presented does, however, indicate that while we already make very efficient devices for some

compositions, there may be harder problems that might be more fundamental in nature for some of the compositions. Among the open questions generated by the current results are whatever or not the phase segregation or trap formation for the bromide rich compositions can be overcome and if the V_{oc} for the pure bromide devices can get closer to what is theoretical obtainable, to which it still is a long way to go.

If the bromide rich perovskites turn out to be inherently unstable, the question arises whatever or not that is true for all the mixed perovskites, and that even the iodide rich ones would decompose if subjected to more stress. At the moment, 1/6 of bromide seems to be about optimal, 2/6 is still rather good, but with more than 50 % bromide we enter what could be called a window of instability. If that window could be decreased, or in reality is larger than what we observe requires further investigations.

From the perspective of tandem devices, the best cells here presented have a band gap that is only slightly lower than what would be optimal for a top cell on silicon. If a higher band gap bottom cell should be used, the compositions that would give the right band gap for the top cell is located in the region where the problem of sub band gap emission and low efficiencies are most pronounced. This illustrates some of the challenges that must be overcome in order to make such tandem devices.

Summary, conclusions, and further outlooks

In this work, the compositional space spanned by $MAPbI_3$, $MAPbBr_3$, $FAPbI_3$ and $FAPbBr_3$ was explored. 49 different perovskite compositions were made by independently varying the MA/FA and the I/Br-ratio. The optical and crystallographic properties of these perovskites were investigated and solar cells were made and characterized.

XRD data indicate that perovskites with a continuous range of iodide/bromide and MA/FA readily can be synthesized over the entire compositional range using a one-step anti-solvent protocol. The spin-coated MA-rich perovskites were found to have a high texture and probably have a tetragonal unit cell, whereas the FA-rich perovskites have a cubic structure and form films with more random crystal orientations.

An increased amount of bromide increases the band gap, whereas an increased amount of FA decreases the band gap but to a smaller extent. Interestingly, the bromide rich compounds have a more excitonic absorption. Based on absorption data, an empirical relation between the band gap and the perovskite composition was derived, which will be highly useful while designing tandem devices.

Perovskite compositions with a high iodide content as well as pure bromide perovskites have a clean PL-spectrum with emission at a single region centered at the band gap energy. For perovskites with a high bromide content, a split in the PL-spectra and intense emission from sub band gap states are observed. These observations appear to be stable over time and are detrimental for device performance. The photoluminescence spectra indicates either the formation of deep trap states or a phase separation with inclusions of an iodide rich minority phase with a lower band gap in a dominant bromide rich phase. XRD and absorption-data does not give direct support for the occurrence of a phase separation, but cannot exclude the formation of small amounts of secondary, iodide rich domains. This illuminates a problem that must be solved for these compositions to be useful in tandem architectures. The exact cause and how the effect can be suppressed will be the focus in further investigations.

In the precursor solutions used for depositing the perovskites a slight excess of lead salts was used, which recently have been shown to be beneficial for device performance. XRD data show that PbI_2, but not $PbBr_2$, is found in the mixed perovskites. That shows that $PbBr_2$ more readily forms the perovskites than PbI_2. This is an insight that could be valuable in the further understanding of the crystallization process for the mixed perovskites, and in the end also

contribute to the understanding of the role played by the PbI_2-excess currently debated in the literature.

Complete solar cell devices were made with all the 49 investigated perovskite compositions. The efficiencies vary over a broad ranch, illustrating that a small change in the composition can have a huge effect for the device performance. The lowest efficiencies are found for mixed perovskites with a high bromide content, which coincide with a strong sub band gap photoluminescence. The highest efficiencies are found for devices where $1/6^{th}$ of the iodine is replaced by bromide and where 2/3rd of the MA is replaced by FA. The efficiencies of those devices were up to 20.7 %, which at the time of testing was higher than highest certified efficiency found in the record tables from NREL, which at that moment was 20.1 %. Recently, a new record based on these mixed perovskites from our laboratory was certified to 21.02 %[13]. This can certainly be optimized further, and by changing the deposition protocol, other compositions can most likely be taken to efficiencies closer to this level. The present work illustrates the importance of the precise composition of the perovskite for making high efficiency devices, and illuminate some problems with trap formation and intense sub band gap recombination for bromide rich devices.

Supporting information

The concentration of the all relevant compounds in all 49 precursor solutions. More general discussion of basic perovskite crystallography. Crystallographic data for PbI_2 and $PbBr_2$. The theoretical evaluation of the performance of tandem cells as a function of band gap which gives the data for figure 4 and 5. Calculated DOS, PDOS, and tilting angles for the four corner compounds. Absorption curves for all samples. A comparison of absorption for different MA/FA-rations and for different Br/I-ratios. A photo of the films. Band gap determination figures for all samples. Error estimations for the empirical relation between band gap and composition. Photoluminescence data for all samples, both normalized data and raw data. Additional SEM figures. XRD data for all compositions. Additional XRD figures. Unit cell parameters as a function of composition. IV-curves for all compositions. Additional device parameters. As separate files are the complete datasets for the absorption, photoluminescence, and XRD measurements. This information is available free of charge at **…..**

Acknowledgements

GRAPHENE project supported by the European Commission Seventh Framework Program under contract 604391 is gratefully acknowledged. We acknowledge Uppsala Multidisciplinary Center for Advanced Computational Science (UPPMAX) for providing the computational resources under projects snic2015-6-65 and snic 2015-1-281.

References

1. D. Weber, *Z. Naturforsch. B*, 1978, **33**, 1443-1445.
2. D. Weber, *Z. Naturforsch. B*, 1978, **33**, 862-865.
3. Z.-K. Tan, R. S. Moghaddam, M. L. Lai, P. Docampo, R. Higler, F. Deschler, M. Price, A. Sadhanala, L. M. Pazos, D. Credgington, F. Hanusch, T. Bein, H. J. Snaith and R. H. Friend, *Nat. Nanotechnol.*, 2014, **9**, 687-692.
4. F. Deschler, M. Price, S. Pathak, L. E. Klintberg, D.-D. Jarausch, R. Higler, S. Huettner, T. Leijtens, S. D. Stranks, H. J. Snaith, M. Atatuere, R. T. Phillips and R. H. Friend, *J. Phys. Chem. Lett*, 2014, **5**, 1421-1426.
5. M. Saliba, Wood, S. M., Patel, J. B., Nayak, P. K., Huang, J., Alexander-Webber, J. A., Wenger, B., Stranks, S. D., Hörantner, M. T., Wang, J. T.-W., Nicholas, R. J., Herz, L. M., Johnston, M. B., Morris, S. M., Snaith, H. J. and Riede, M. K. , *Adv. Mater.*, 2015.
6. K. Domanski, W. Tress, T. Moehl, M. Saliba, M. K. Nazeeruddin and M. Grätzel, *Adv. Funct. Mater.*, 2015, **25**, 6936-6947.
7. A. Kojima, K. Teshima, Y. Shirai and T. Miyasaka, *JACS.*, 2009, **131**, 6050-6051.
8. J. H. Im, C. R. Lee, J. W. Lee, S. W. Park and N. G. Park, *Nanoscale*, 2011, **3**, 4088-4093.
9. M. M. Lee, J. Teuscher, T. Miyasaka, T. N. Murakami and H. J. Snaith, *Science*, 2012, **338**, 643-647.
10. H. S. Kim, C. R. Lee, J. H. Im, K. B. Lee, T. Moehl, A. Marchioro, S. J. Moon, R. Humphry-Baker, J. H. Yum, J. E. Moser, M. Gratzel and N. G. Park, *Sci. Rep.*, 2012, **2**, 1-7.
11. J. H. Heo, S. H. Im, J. H. Noh, T. N. Mandal, C. S. Lim, J. A. Chang, Y. H. Lee, H. J. Kim, A. Sarkar, M. K. Nazeeruddin, M. Gratzel and S. I. Seok, *Nat. Photonics*, 2013, **7**, 487-492.
12. J. Burschka, N. Pellet, S. J. Moon, R. Humphry-Baker, P. Gao, M. K. Nazeeruddin and M. Gratzel, *Nature*, 2013, **499**, 316-319.
13. , Laboratory of Photomolecular Science and Laboratory of Photonics and Interfaces, École Polytechnique Fédérale de Lausanne. Certified efficiency measurement by the laboratories of Newport Corporation in Bozeman, Montana, on December 1, 2015.
14. T. M. Koh, K. Fu, Y. Fang, S. Chen, T. C. Sum, N. Mathews, S. G. Mhaisalkar, P. P. Boix and T. Baikie, *J. Phys. Chem. C*, 2014, **118**, 16458-16462.
15. N. Pellet, P. Gao, G. Gregori, T.-Y. Yang, M. K. Nazeeruddin, J. Maier and M. Graetzel, *Angew. Chem. Int. Edit.*, 2014, **53**, 3151-3157.
16. J.-W. Lee, D.-J. Seol, A.-N. Cho and N.-G. Park, *Adv. Mater.*, 2014, **26**, 4991-4998.
17. W. S. Yang, J. H. Noh, N. J. Jeon, Y. C. Kim, S. Ryu, J. Seo and S. I. Seok, *Science*, 2015, **348**, 1234-1237.
18. M. Hu, L. Liu, A. Mei, Y. Yang, T. Liu and H. Han, *J. Mater. Chem. Chem. A*, 2014, **2**, 17115-17121.
19. A. Binek, F. C. Hanusch, P. Docampo and T. Bein, *J. Phys. Chem. Lett*, 2015, **6**, 1249-1253.
20. M. Kulbak, D. Cahen and G. Hodes, *J. Phys. Chem. Lett*, 2015, **6**, 2452-2456.
21. C. Yi, J. Luo, S. Meloni, A. Boziki, N. Ashari-Astani, C. Gratzel, S. M. Zakeeruddin, U. Rothlisberger and M. Gratzel, *Energ. Environ. Sci.*, 2015.
22. H. Choi, J. Jeong, H.-B. Kim, S. Kim, B. Walker, G.-H. Kim and J. Y. Kim, *Nano Energy*, 2014, **7**, 80-85.
23. J.-W. Lee, D.-H. Kim, H.-S. Kim, S.-W. Seo, S. M. Cho and N.-G. Park, *Adv. Energ. Mater.*, 2015, **5**.

24. O. Knop, R. E. Wasylishen, M. A. White, T. S. Cameron and M. J. M. Vanoort, *Can. J. Chem.-Rev. Can. Chim.*, 1990, **68**, 412-422.
25. J. H. Heo, D. H. Song and S. H. Im, *Adv. Mater.*, 2014, **26**, 8179-8183.
26. E. T. Hoke, D. J. Slotcavage, E. R. Dohner, A. R. Bowring, H. I. Karunadasa and M. D. McGehee, *Chem. Sci.*, 2015, **6**, 613-617.
27. S. Aharon, B. El Cohen and L. Etgar, *J. Phys. Chem. C*, 2014, **118**, 17160-17165.
28. A. Sadhanala, F. Deschler, T. H. Thomas, S. E. Dutton, K. C. Goedel, F. C. Hanusch, M. L. Lai, U. Steiner, T. Bein, P. Docampo, D. Cahen and R. H. Friend, *J. Phys. Chem. Lett*, 2014, **5**, 2501-2505.
29. G. E. Eperon, S. D. Stranks, C. Menelaou, M. B. Johnston, L. M. Herz and H. J. Snaith, *Energ. Environ. Sci.*, 2014, **7**, 982-988.
30. H. Yu, F. Wang, F. Xie, W. Li, J. Chen and N. Zhao, *Adv. Funct. Mater.*, 2014, **24**, 7102-7108.
31. J. P. C. Baena, L. Steier, W. Tress, M. Saliba, S. Neutzner, T. Matsui, F. Giordano, T. J. Jacobsson, A. R. S. Kandada, S. M. Zakeeruddin, A. Petrozza, A. Abate, M. K. Nazeeruddin, M. Graetzel and A. Hagfeldt, *Energ. Environ. Sci.*, 2015, **8**, 2928-2934.
32. N. J. Jeon, J. H. Noh, W. S. Yang, Y. C. Kim, S. Ryu, J. Seo and S. I. Seok, *Nature*, 2015, **517**, 476-+.
33. T. J. Jacobsson and T. Edvinsson, *Inorg. Chem.*, 2011, **50**, 9578-9586.
34. H. J. Snaith, *J. Phys. Chem. Lett*, 2013, **4**, 3623-3630.
35. C. D. Bailie, M. G. Christoforo, J. P. Mailoa, A. R. Bowring, E. L. Unger, W. H. Nguyen, J. Burschka, N. Pellet, J. Z. Lee, M. Graetzel, R. Noufi, T. Buonassisi, A. Salleo and M. D. McGehee, *Energ. Environ. Sci.*, 2015, **8**, 956-963.
36. I. Almansouri, A. Ho-Baillie and M. A. Green, *Jpn. J. Appl. Phys.*, 2015, **54**.
37. C. D. Bailie and M. D. McGehee, *Mrs Bull.*, 2015, **40**, 681-685.
38. M. Filipic, P. Loeper, B. Niesen, S. De Wolf, J. Krc, C. Ballif and M. Topic, *Opt. Express*, 2015, **23**, A263-A278.
39. P. Loeper, S.-J. Moon, S. M. de Nicolas, B. Niesen, M. Ledinsky, S. Nicolay, J. Bailat, J.-H. Yum, S. De Wolf and C. Ballif, *Phys. Chem. Chem. Phys.*, 2015, **17**, 1619-1629.
40. S. Albrecht, M. Saliba, J. P. Correa Baena, F. Lang, L. Kegelmann, M. Mews, L. Steier, A. Abate, J. Rappich, L. Korte, R. Schlatmann, M. K. Nazeeruddin, A. Hagfeldt, M. Gratzel and B. Rech, *Energ. Environ. Sci.*, 2016.
41. F. Giordano, A. Abate, J. P. Correa Baena, M. Saliba, T. Matsui, S. H. Im, S. M. Zakeeruddin, M. K. Nazeeruddin, A. Hagfeldt and M. Graetzel, *Nat Commun*, 2016, **7**.
42. C. Roldan-Carmona, P. Gratia, I. Zimmermann, G. Grancini, P. Gao, M. Graetzel and M. K. Nazeeruddin, *Energ. Environ. Sci.*, 2015, **8**, 3550-3556.
43. Q. Chen, H. Zhou, T.-B. Song, S. Luo, Z. Hong, H.-S. Duan, L. Dou, Y. Liu and Y. Yang, *Nano Letters*, 2014, **14**, 4158-4163.
44. L. Wang, C. McCleese, A. Kovalsky, Y. Zhao and C. Burda, *JACS.*, 2014, **136**, 12205-12208.
45. V. Somsongkul, F. Lang, A. R. Jeong, M. Rusu, M. Arunchaiya and T. Dittrich, *Phys. Status Solidi-R.*, 2014, **8**, 763-766.
46. Y. Zhao and K. Zhu, *J. Phys. Chem. Lett*, 2014, **5**, 4175-4186.
47. M. Xiao, F. Huang, W. Huang, Y. Dkhissi, Y. Zhu, J. Etheridge, A. Gray-Weale, U. Bach, Y.-B. Cheng and L. Spiccia, *Angew. Chem. Int. Edit.*, 2014, **53**, 9898-9903.
48. N. J. Jeon, J. H. Noh, Y. C. Kim, W. S. Yang, S. Ryu and S. Il Seol, *Nat. Mater.*, 2014, **13**, 897-903.

49. A. Abate, T. Leijtens, S. Pathak, J. Teuscher, R. Avolio, M. E. Errico, J. Kirkpatrik, J. M. Ball, P. Docampo, I. McPherson and H. J. Snaith, *Phys. Chem. Chem. Phys.*, 2013, **15**, 2572-2579.
50. A. Abate, D. R. Staff, D. J. Hollman, H. J. Snaith and A. B. Walker, *Phys. Chem. Chem. Phys.*, 2014, **16**, 1132-1138.
51. J. P. Perdew, K. Burke and M. Ernzerhof, *Phys. Rev. Lett.*, 1996, **77**, 3865-3868.
52. E. Mosconi, A. Amat, M. K. Nazeeruddin, M. Graetzel and F. De Angelis, *J. Phys. Chem. C*, 2013, **117**, 13902-13913.
53. C. Quarti, E. Mosconi and F. De Angelis, *Chem. Mater.*, 2014, **26**, 6557-6569.
54. F. C. Hanusch, E. Wiesenmayer, E. Mankel, A. Binek, P. Angloher, C. Fraunhofer, N. Giesbrecht, J. M. Feckl, W. Jaegermann, D. Johrendt, T. Bein and P. Docampo, *J. Phys. Chem. Lett*, 2014, **5**, 2791-2795.
55. M. Hu, C. Bi, Y. Yuan, Z. Xiao, Q. Dong, Y. Shao and J. Huang, *Small*, 2015, **11**, 2164-2169.
56. C. Sheng, C. Zhang, Y. Zhai, K. Mielczarek, W. Wang, W. Ma, A. Zakhidov and Z. V. Vardeny, *Phys. Rev. Lett.*, 2015, **114**.
57. T. J. Jacobsson and T. Edvinsson, *J. Phys. Chem. C*, 2012, **116**, 15692-15701.
58. M. Fondell, T. J. Jacobsson, M. Boman and T. Edvinsson, *J. Mater. Chem. A*, 2014.
59. T. J. Jacobsson and T. Edvinsson, *J. Phys. Chem. C*, 2014, **118**, 12061-12072.
60. M. R. Filip, G. E. Eperon, H. J. Snaith and F. Giustino, *Nat Commun*, 2014, **5**.
61. W. Geng, L. Zhang, Y.-N. Zhang, W.-M. Lau and L.-M. Liu, *J. Phys. Chem. C*, 2014, **118**, 19565-19571.
62. T. J. Jacobsson, M. Pazoki, A. Hagfeldt and T. Edvinsson, *J. Phys. Chem. C*, 2015.
63. C. Quarti, E. Mosconi, J. M. Ball, V. D'Innocenzo, C. Tao, S. Pathak, H. J. Snaith, A. Petrozza and F. De Angelis, *Energ. Environ. Sci.*, 2016.
64. Y. Zhao, A. M. Nardes and K. Zhu, *J. Phys. Chem. Lett*, 2014, **5**, 490-494.
65. N. Kedem, T. M. Brenner, M. Kulbak, N. Schaefer, S. Levcenko, I. Levine, D. Abou-Ras, G. Hodes and D. Cahen, *J. Phys. Chem. Lett*, 2015, **6**, 2469-2476.
66. D. Bi, W. Tress, M. I. Dar, P. Gao, J. Luo, C. Renevier, K. Schenk, A. Abate, F. Giordano, J.-P. Correa Baena, J.-D. Decoppet, S. M. Zakeeruddin, M. K. Nazeeruddin, M. Grätzel and A. Hagfeldt, *Sci. Adv.*, 2016, **2**.
67. V. M. Goldschmidt, *Naturwissenschaften*, 1926, **14**, 477-485.
68. T. J. Jacobsson, L. J. Schwan, M. Ottosson, A. Hagfeldt and T. Edvinsson, *Inorg. Chem.*, 2015, **54**, 10678-10685.
69. N. K. McKinnon, D. C. Reeves and M. H. Akabas, *J. Gen. Physiol.*, 2011, **138**, 453-466.
70. Y. Y. Dang, Y. Liu, Y. X. Sun, D. S. Yuan, X. L. Liu, W. Q. Lu, G. F. Liu, H. B. Xia and X. T. Tao, *Crystengcomm*, 2015, **17**, 665-670.
71. Q. Dong, Y. Fang, Y. Shao, P. Mulligan, J. Qiu, L. Cao and J. Huang, *Science*, 2015, **347**, 967-970.
72. D. Shi, V. Adinolfi, R. Comin, M. Yuan, E. Alarousu, A. Buin, Y. Chen, S. Hoogland, A. Rothenberger, K. Katsiev, Y. Losovyj, X. Zhang, P. A. Dowben, O. F. Mohammed, E. H. Sargent and O. M. Bakr, *Science*, 2015, **347**, 519-522.
73. P. Zhao, J. Xu, X. Dong, L. Wang, W. Ren, L. Bian and A. Chang, *J. Phys. Chem. Lett*, 2015, **6**, 2622-2628.
74. M. F. Aygueler, M. D. Weber, B. M. D. Puscher, D. D. Medina, P. Docampo and R. D. Costa, *J. Phys. Chem. C*, 2015, **119**, 12047-12054.
75. S. Pang, H. Hu, J. Zhang, S. Lv, Y. Yu, F. Wei, T. Qin, H. Xu, Z. Liu and G. Cui, *Chem. Mater.*, 2014, **26**, 1485-1491.

76. S. Lv, S. Pang, Y. Zhou, N. P. Padture, H. Hu, L. Wang, X. Zhou, H. Zhu, L. Zhang, C. Huang and G. Cui, *Phys. Chem. Chem. Phys.*, 2014, **16**, 19206-19211.
77. C. C. Stoumpos, C. D. Malliakas and M. G. Kanatzidis, *Inorg. Chem.*, 2013, **52**, 9019-9038.
78. E. Edri, S. Kirmayer, M. Kulbak, G. Hodes and D. Cahen, *J. Phys. Chem. Lett*, 2014, **5**, 429-433.
79. R. S. Sanchez, V. Gonzalez-Pedro, J.-W. Lee, N.-G. Park, Y. S. Kang, I. Mora-Sero and J. Bisquert, *J. Phys. Chem. Lett*, 2014, **5**, 2357-2363.
80. H.-S. Kim and N.-G. Park, *J. Phys. Chem. Lett*, 2014, **5**, 2927-2934.
81. H. J. Snaith, A. Abate, J. M. Ball, G. E. Eperon, T. Leijtens, N. K. Noel, S. D. Stranks, J. T.-W. Wang, K. Wojciechowski and W. Zhang, *J. Phys. Chem. Lett*, 2014, **5**, 1511-1515.
82. E. L. Unger, E. T. Hoke, C. D. Bailie, W. H. Nguyen, A. R. Bowring, T. Heumueller, M. G. Christoforo and M. D. McGehee, *Energ. Environ. Sci.*, 2014, **7**, 3690-3698.
83. J. M. Azpiroz, E. Mosconi, J. Bisquert and F. De Angelis, *Energ. Environ. Sci.*, 2015, **8**, 2118-2127.
84. A. K. Jena, H.-W. Chen, A. Kogo, Y. Sanehira, M. Ikegami and T. Miyasaka, *Asc Apl. Mater. Inter.*, 2015, **7**, 9817-9823.
85. J. M. Frost, K. T. Butler and A. Walsh, *Apl Materials*, 2014, **2**.
86. J. A. Christians, J. S. Manser and P. V. Kamat, *J. Phys. Chem. Lett*, 2015, **6**, 852-857.
87. P. Umari, E. Mosconi and F. De Angelis, *Sci. Rep.*, 2014, **4**.
88. T. J. Jacobsson and T. Edvinsson, *J. Phys. Chem. C*, 2013, **117**, 5497-5504.
89. M. Pazoki, N. Nafari and N. Taghavinia, *Rsc Advances*, 2014, **4**, 301-307.
90. A. Calloni, A. Abate, G. Bussetti, G. Berti, R. Yivlialin, F. Ciccacci and L. Duo, *J. Phys. Chem. C*, 2015, **119**, 21329-21335.
91. M. A. Green, A. Ho-Baillie and H. J. Snaith, *Nat Photon*, 2014, **8**, 506-514.
92. P. Schulz, E. Edri, S. Kirmayer, G. Hodes, D. Cahen and A. Kahn, *Energ. Environ. Sci.*, 2014, **7**, 1377-1381.
93. J. Haruyama, K. Sodeyama, L. Han and Y. Tateyama, *JACS*, 2015, **137**, 10048-10051.